Supporting Information for:

# Tuning the Bandgap of $Cs_2AgBiBr_6$ Through Dilute Tin Alloying

Kurt P. Lindquist,[a] Stephanie A. Mack,[bc] Adam H. Slavney,[a] Linn Leppert,[d] Aryeh Gold-Parker,[ae] Jonathan F. Stebbins,[f] Alberto Salleo,[g] Michael F. Toney,[e] Jeffrey B. Neaton,[bch] and Hemamala I. Karunadasa*[ai]

[a]*Department of Chemistry, Stanford University, Stanford, California 94305, USA*
[b]*Molecular Foundry, Lawrence Berkeley National Laboratory, Berkeley, California 94720, USA*
[c]*Department of Physics, University of California Berkeley, Berkeley, California 94720, USA*
[d]*Department of Physics, University of Bayreuth, 95440 Bayreuth, Germany*
[e]*Stanford Synchrotron Radiation Lightsource, SLAC National Accelerator Laboratory, Menlo Park, California 94025, USA*
[f]*Department of Geological Sciences, Stanford University, Stanford, California 94305, USA*
[g]*Department of Materials Science and Engineering, Stanford University, Stanford, California 94305, USA*
[h]*Kavli Energy NanoScience, Institute at Berkeley, Berkeley, California 94720, USA*
[i]*Stanford Institute for Materials and Energy Sciences, SLAC National Accelerator Laboratory, Menlo Park, California 94025, USA*

**hemamala@stanford.edu*

**Experimental methods**

All manipulations were performed in a $N_2$- or Ar-filled glovebox unless otherwise noted. Solvents were of reagent grade or higher purity. All reagents were purchased from commercial vendors and used as received unless otherwise noted. The solvents dimethyl sulfoxide (DMSO) and *n*-hexane were dried and degassed using the JC Meyer solvent purification system. The solvent ethanol was degassed under $N_2$ and dried using 3 Å molecular sieves. Crystals of $Cs_2AgBiBr_6$ (**1**) were synthesized by a previously reported method.[1]

**Synthesis of crystals of Sn-alloyed $Cs_2AgBiBr_6$ (1:Sn)**

Solids CsBr (362 mg, 1.70 mmol), $BiBr_3$ (381 mg, 0.850 mmol), AgBr (160 mg, 0.850 mmol), and $SnBr_2$ (ranging from 2.4 mg, 0.0085 mmol to 474 mg, 1.70 mmol) were combined in a 20 mL scintillation vial with 10 mL of HBr. This solution was heated to 110 ºC and kept at that temperature for ~2 h until the red or black solid fully dissolved into a clear yellow solution. An insoluble beige precipitate identified as $Cs_2Sn^{IV}Br_6$ was present in the vial; its quantity was proportional to the amount of $SnBr_2$ present in the reaction. The temperature was then lowered to room temperature at an approximate rate of 5 ºC/h, resulting in the precipitation of red to black crystals of **1:Sn** with dimensions on the order of hundreds of microns. The crystals were separated from the mother liquor by filtration over a glass microfiber filter. The byproduct $Cs_2Sn^{IV}Br_6$ was a very finely divided powder and infiltrated the glass microfiber filter and was therefore easily mechanically separated from the crystals of **1:Sn**. The crystals were then rinsed with fresh HBr and subsequently dried under reduced pressure.

The use of purified $SnBr_2$ and HBr (see **Reagent purification**) and the addition of hypophosphorous acid (2 mL of a 50 wt.% in $H_2O$ solution) could sometimes reduce the amount of $Cs_2SnBr_6$ impurity in these crystallizations of **1:Sn**. The crystals of **1:Sn** produced with purified reagents appeared identical to those produced without reagent purification. The inclusion of $Sn^0$ powder in the crystallization solution for **1:Sn** in HBr was successful in preventing the formation of $Cs_2Sn^{IV}Br_6$. However, $Sn^0$ reacts with HBr to form $SnBr_2$ and $H_2$, thus addition of $Sn^0$ added uncertainty to the concentration of $Sn^{2+}$ in the crystallization solution. Additionally, separation of crystals of **1:Sn** from unreacted $Sn^0$ proved difficult. When $Sn^0$ was used as the only source of Sn to control for the $Sn^{2+}$ concentration, the solution had to be heated at reflux for ~8 h for the reaction of $Sn^0$ with HBr to reach completion, which led to the oxidation of $Sn^{2+}$ and the formation of $Cs_2Sn^{IV}Br_6$. Attempts to synthesize crystals of **1:Sn** using DMSO as the solvent resulted in the formation of phase-impure mixtures of **1:Sn** and various side-products, such as $CsAgBr_2$. Addition of $SnBr_4$ to the precursor solution for **1** or **1:Sn** resulted in a biphasic mixture of $Cs_2Sn^{IV}Br_6$ and **1** or **1:Sn**. Exposure of the precursor solution for **1:Sn** to ambient atmosphere during synthesis resulted in oxidation of $Sn^{2+}$ to form **1** and $Cs_2Sn^{IV}Br_6$.

**Synthesis of $CsSn^{II}Br_3$ powder**

The synthesis of $CsSn^{II}Br_3$ was adapted from a previously reported method.[2] Solids CsBr (426 mg, 2.00 mmol) and $SnBr_2$ (557 mg, 2.00 mmol) were combined in a 4 mL vial. Upon addition of 1 mL HBr, a black solid immediately formed. This suspension was stirred at 100 ºC for ~0.5 h. The slurry was allowed to cool to room temperature before the black solid was separated from the mother liquor by filtration over a glass

microfiber filter. The powder was rinsed with fresh HBr and subsequently dried under reduced pressure. The purity of the product was confirmed by powder X-ray diffraction (PXRD).

**Synthesis of $Cs_2Sn^{IV}Br_6$ powder**

The synthesis of $Cs_2Sn^{IV}Br_6$ was adapted from a previously reported method.[3] Solids CsBr (426 mg, 2.00 mmol) and $SnBr_4$ (438 mg, 1.00 mmol) were combined in a 4 mL vial. Upon addition of 1 mL HBr, a beige solid immediately formed. This suspension was stirred at 100 ºC for ~0.5 h. The slurry was allowed to cool to room temperature before the beige solid was separated from the mother liquor by filtration over a glass microfiber filter. The powder was rinsed with fresh HBr and subsequently dried under reduced pressure. The purity of the product was confirmed by PRXD.

**Film deposition**

*Substrate preparation.* Films were spincoated onto glass, fused silica, or silicon substrates under inert atmosphere. Before spincoating, substrates were cleaned by scrubbing with an aqueous Sparkleen® detergent solution, then sonicated for 10 minutes each in aqueous Sparkleen® solution, deionized water, acetone, and then isopropanol. Upon removal from the isopropanol bath, the substrates were dried with pressurized air. Immediately prior to spincoating, the cleaned substrates were subjected to a 15-minute UV-ozone treatment and taken into a $N_2$-filled glove box containing a spincoater.

*Solution preparation.* For films of **1**, crystals of **1** (266 mg, 0.250 mmol) were dissolved in 0.5 mL DMSO. For films of **1:Sn**, crystals of **1** (212–252 mg, 0.200–0.238 mmol) and crystals of $CsSn^{II}Br_3$ (12.3–49.1 mg, 0.0125–0.0500 mmol) were dissolved together in 0.5 mL DMSO. The mixture of **1** and $CsSn^{II}Br_3$ was kept such that the concentrations of Cs and Br in the resulting solutions remained constant at 0.5 M and 1.5 M, respectively. In each case, the solution was heated at 100 ºC for ~2 h with occasional agitation until the solid was fully dissolved and the solution was a clear yellow color. The solution was then allowed to cool to room temperature before filtering through a syringe plugged with a glass microfiber filter paper.

*Spincoating.* The solution was heated to 100 ºC then 10–60 µL were deposited onto the substrate. The volume of solution used depended on the size of the substrate, ranging from 10 µL for a 0.5 × 0.5 $cm^2$ substrate to 60 µL for a 2.5 × 2.5 $cm^2$ substrate. After the solution was deposited onto the substrate, it was spun at 500 rpm for 30 s (acceleration of 100 rpm/s) then at 5000 rpm for 45 s (acceleration of 4000 rpm/s). During the second spinning step at 5000 rpm, $N_2$ was blown inside the spincoater against the side wall to increase airflow and accelerate solvent evaporation. Immediately upon completion of spinning, the film was annealed at 200 ºC for 5 minutes.

*Thickness determination.* Film thickness was measured using a Bruker Dektak XT stylus profiler.

**Reagent purification**

*$SnBr_2$.* Solid $SnBr_2$ (1.114 g, 4.000 mmol) was added to 0.85 mL ethanol and dissolved at 70 ºC. The solution was filtered at 70 ºC through a syringe plugged with a glass microfiber filter paper. The solution was then allowed to cool to room temperature. The addition of 4 mL *n*-hexane to the solution afforded a

colorless solid, which was isolated through filtration and dried under reduced pressure. The solid $SnBr_2$ was stored in a $N_2$-filled glove box in a dark container.

*Hydrobromic acid.* Commercial HBr was fractionally distilled in ambient atmosphere. The constant-boiling azeotrope (48 wt.% in $H_2O$, 8.9 M) at 126 ºC was kept and the first and last 5–10 mL fractions were discarded. The distillation product was colorless, having lost the yellow color of the as-received hydrobromic acid. The distillation was repeated three times to ensure purity.

**Iodimetric titration**

An iodimetric titration was performed on **1:Sn** to confirm the concentration of $Sn^{2+}$ in the solid. Titration of $CsSn^{II}Br_3$ was also performed as a control. The titration involves the oxidation of $Sn^{2+}$ by $I_2$ generated *in situ*, followed by the back-titration of the remaining $I_2$ with $S_2O_3^{2-}$, according to the following scheme:

$$IO_3^- + 5I^- + 6H^+ \leftrightarrow 3I_2 + 3H_2O$$

$$I_2 + Sn^{2+} \rightarrow 2I^- + Sn^{4+}$$

$$2S_2O_3^{2-} + I_2 \rightarrow S_4O_6^{2-} + 2I^-$$

Given a known concentration of $IO_3^-$ and $S_2O_3^{2-}$ and an excess of $I^-$ and $H^+$, the amount of $I_2$ reduced to $I^-$ by the sample and therefore the concentration of $Sn^{2+}$ in the sample can be determined. The advantages of this titration method are, first, that the $I_2$ will selectively oxidize $Sn^{2+}$ and will not oxidize any other ions present in **1:Sn**, second, that the $Sn^{2+}$ is quickly oxidized by $I_2$ upon addition of **1:Sn** to the titration solution, thus allowing the experiment to be performed in ambient atmosphere without the concern of atmospheric oxidation of $Sn^{2+}$ during the course of the titration, and, third, that the $I_2$ itself provides a simple colorimetric indicator, aided by the addition of a starch indicator solution.[4]

Prior to sample preparation, all glassware was cleaned by soaking in aqua regia overnight, followed by rinsing 5 times with deionized water. All solutions were prepared on the day the titration was performed to avoid decomposition, particularly of $Na_2S_2O_3$(aq). The $Na_2S_2O_3$ titrant was standardized against the $KIO_3$ solution three times before titration of the samples and once after titration of the samples to determine the concentration of $Na_2S_2O_3$ and rule out degradation over the course of the experiment. Solids **1:Sn** (1 atom% Sn) and $CsSn^{II}Br_3$ were digested in triply distilled HBr at concentrations of 30 mM. The $CsSn^{II}Br_3$ solution was then diluted by a factor of 10 using Milli-Q water (18.2 MΩ·cm resistivity at 25 °C). Solutions of $Na_2S_2O_3$ (1.8 mM) and $KIO_3$ (10 mM) were prepared in ambient atmosphere using volumetric glassware. To 30 mL Milli-Q water, 1 mL of $KIO_3$ solution and 100 mg KI were added. The solution was degassed with $N_2$ gas for ~30 min prior to the addition of the samples. Digested samples of **1:Sn** and $CsSn^{II}Br_3$ were removed from the glovebox and added to the degassed $KIO_3$/KI solution. The formation of a small amount of green precipitate, assumed to be a silver halide salt, was observed upon addition of **1:Sn** to the $KIO_3$/KI solution. The resulting solution was stirred while it was titrated with the $Na_2S_2O_3$ solution in ambient atmosphere. The titrant was added until the yellow-brown color became faint, at which point 1 mL of a starch indicator solution was added to the solution being titrated. The solution was then titrated until the

purple-blue color disappeared completely, at which point the endpoint was recorded. Each sample was run in triplicate to ensure reproducibility.

**Crystal structure determination**

Crystals of **1:Sn** were mounted on a Kapton® loop using Paratone-N® oil. To minimize degradation of the samples, the crystals were removed from inert atmosphere immediately prior to transferring to the oil for selection. The crystal was then transferred to the Bruker D85 diffractometer at the Advanced Light Source beamline 11.3.1 equipped with a Photon 100 CMOS detector at Lawrence Berkeley National Laboratory or to the Bruker D8 Venture diffractometer equipped with a Photon II CCD detector at the Stanford Nano Shared Facilities. Frames were collected using ω and ψ scans with synchrotron radiation (18.000 keV, λ = 0.68880 Å) or Mo-Kα radiation (17.445 keV, λ = 0.71073 Å). Unit-cell parameters were refined against all data. The crystals did not show significant decay during data collection. Frames were integrated and corrected for Lorentz and polarization effects using SAINT 8.37a or 8.38a and were corrected for absorption effects using SADABS V2016/2.[5] Space-group assignments were based upon systematic absences, *E*-statistics, agreement factors for equivalent reflections, and successful refinement of the structures. The structure was solved by direct methods, expanded through successive difference Fourier maps using SHELXS, and refined against all data using the SHELXL-2014[6] software package as implemented in Olex2.[6-9] Weighted *R* factors, $R_w$, and all goodness-of-fit indicators are based on $F^2$. Thermal parameters for all atoms were refined anisotropically. The refinement parameters are listed in Table S2.

Crystal structures were collected for a crystal of **1:Sn** (1 atom% Sn) obtained from a batch of phase-pure crystals of **1:Sn** and for a crystal of **1:Sn** taken from a batch of crystals synthesized with a sufficiently high concentration of Sn that it contained a mixture of **1:Sn** and $CsSn^{II}Br_3$. Refinement of **1:Sn** (phase-pure) with full Ag and Bi occupancies resulted in a large electron density hole at the Ag site, while refinement of **1:Sn** (phase-impure) with full Ag and Bi occupancies resulted in a larger electron density hole at the Ag site and a small electron hole at the Bi site. The electron density hole at the Bi site in the phase-impure sample suggests that Sn substitution occurs at the Bi site in **1:Sn**, though its low concentration in the phase-pure crystal likely precludes indications of its presence from rising above the noise. We modelled mixed occupancy of the Ag site in both solutions using the SUMP instruction of SHELXL and assuming each substitution of Sn for Ag produced a Ag vacancy. For the phase-pure crystal, this model provided a Ag occupancy of 86% and a Sn occupancy of 7.0% at the Ag site, leaving 7.0% of the Ag sites vacant. The concentration of Sn determined by this method (0.70 atom%) is within error of that determined by ICP analysis, supporting the proposed substitution mechanism. For the phase-impure crystal, this model provided a Ag occupancy of 65% and a Sn occupancy of 18% at the Ag site, leaving 18% of the Ag sites vacant. Additionally, the Bi site in the phase-impure crystal can be modelled as a mixed-atom site with a 84% occupancy of Bi and 16% occupancy of Sn.

**Powder X-ray diffraction**

PXRD data were collected using a Bruker D8 Advance diffractometer equipped with a Cu anode, fixed divergence slits with a nickel filter, and a LYNXEYE 1D detector. The instrument was operated in a Bragg-Brentano geometry with a step size of 0.008° (2θ). Powder samples were prepared by coating a glass cover slide with grease and adhering the powder to the grease. PXRD measurements were performed in ambient atmosphere; to minimize degradation of the samples, the samples were removed from inert atmosphere

immediately prior to preparation and measurement. Simulated powder patterns were calculated using the crystallographic information files (CIFs) from single-crystal X-ray experiments.

**X-ray photoelectron spectroscopy (XPS)**

XPS data were collected using a PHI Versaprobe 3 equipped with a focused Ar ion gun (FIG), electron gun, and an Ar 2500+ gas cluster ion beam gun (GCIB). Thin film samples of **1** and **1:Sn** were prepared on doped-Si substrates to minimize charging effects. Samples were mounted to the sample stage using Cu clips. Exposure of the samples to ambient atmosphere was limited to under 60 s during the sample mounting and loading process. Survey scans were obtained with a pass energy of 224 eV. High-resolution scans were obtained of C-1s, Cs-3d, Ag-3d, Bi-4f, Sn-3d, and Br-3d signals using a pass energy of 55 eV. The films were neutralized using the FIG and electron gun. The film surfaces were sputtered with the GCIB over a 2 × 2 $mm^2$ area. The beam current was 10 nA and the voltage was 2.5 kV. Sputtering was performed for 1 min. Scans were taken both before and after sputtering for comparison. The relative concentration of Sn decreased slightly upon sputtering, consistent with slight oxidation of $Sn^{2+}$.[10] Elemental quantification was performed using the MultiPak v.9.6.0 XPS analysis software. The high-resolution scans of each element were fit using a mixture of Gaussian and Lorentzian functions and the area under the peak(s) determined and compared with the total area under all the element peaks. There was some sample-to-sample variation, attributed to error inherent to the technique. Spectra were aligned using the C-1s peak of adventitious carbon.

**X-ray absorption spectroscopy**

*Sn K-edge.* X-ray absorption near-edge structure (XANES) spectra were collected at the K-edge of Sn at beamline 4-1 at the Stanford Synchrotron Radiation Lightsource (SSRL). Crystal samples of **1:Sn** were ground using a mortar and pestle. Powder samples of $CsSn^{II}Br_3$ and $Cs_2Sn^{IV}Br_6$ were diluted in a mull with hexagonal BN by factors of 24 and 13, by mass, respectively. Samples were packed into 1 mm thick aluminum pallets and encapsulated using Kapton® tape. All sample manipulations were performed under inert atmosphere. To avoid leakage of ambient atmosphere through the Kapton® encapsulant, samples were kept sealed in glass jars under inert atmosphere until transfer into the sample measurement chamber. The sample measurement chamber was continuously purged with Ar to avoid sample decomposition. Transmission spectra were collected for $CsSn^{II}Br_3$ and $Cs_2Sn^{IV}Br_6$. Fluorescence spectra were collected for all samples using a Canberra EGPS 30-element Ge detector, narrowing the spectral acceptance window to include only the contribution of the Sn-Kα fluorescence. The spectra from all the detector elements were averaged. In every scan, simultaneous transmission measurements were collected on a Sn reference foil. The spectra were analyzed using the Athena software package.[11] Each spectrum was energy-calibrated by assigning the inflection point on the Sn foil rising edge to 29200 eV. The spectra were then normalized by fitting the pre-edge region to a line and the post-edge to a cubic or quadratic polynomial. The effect of self-absorption on $CsSn^{II}Br_3$ and $Cs_2Sn^{IV}Br_6$ was determined to be insignificant based on the near identity of their respective transmission and fluorescence spectra.

*Sn $L_3$-edge.* XANES spectra were collected at the $L_3$-edge of Sn at beamline 4-3 at SSRL. Crystal samples of **1:Sn** were ground using a mortar and pestle. Powder samples of $CsSn^{II}Br_3$ and $Cs_2Sn^{IV}Br_6$ were diluted in a mull with hexagonal BN by factors of 24 and 13, by mass, respectively. Samples were packed into 1 mm thick aluminum pallets with a backing of Kapton® tape and were encapsulated using a 0.2 mil (5 μm) thick polypropylene film. All sample manipulations were performed under inert atmosphere. To avoid

leakage of ambient atmosphere through the Kapton® and polypropylene film encapsulants, samples were kept sealed in glass jars under inert atmosphere until transfer into the sample measurement chamber. The sample measurement chamber was continuously purged with He to avoid sample decomposition and reduce atmospheric absorption of the X-rays. Transmission spectra were collected for $CsSn^{II}Br_3$ and $Cs_2Sn^{IV}Br_6$. Fluorescence spectra were collected for all samples using a Hitachi Vortex®-ME4 4-element Si drift detector, narrowing the spectral acceptance window to include only the contribution of the Sn-Lα fluorescence. The spectra from all the detector elements were averaged. Transmission measurements were collected on a Sn foil after every 3–5 scans to check the energy calibration. No significant alignment drift was observed. The spectra were analyzed using the Athena software package.[11] Each spectrum was energy-calibrated by assigning the inflection point on the Sn foil rising edge to 3929 eV. The spectra were then normalized by fitting the pre-edge region to a line and the post-edge to a cubic or quadratic polynomial. The effect of self-absorption on $CsSn^{II}Br_3$ and $Cs_2Sn^{IV}Br_6$ was determined to be insignificant based on the near identity of their respective transmission and fluorescence spectra.

**Solid-state NMR**

Solid-state $^{119}Sn$ NMR spectra were collected with a Varian Inova-600 spectrometer at 223.6 MHz Larmor frequency, using a magic-angle spinning (MAS) probe with 3.2 mm zirconia rotors and spinning rates of 10–20 kHz. Spectra were referenced to $SnO_2$ at −604 ppm. Single pulse excitation with 1 μs (ca. 30˚ rf tip angle) pulses and a 60 s pulse delay were typically used because of the expected slow spin-lattice relaxation for this nuclide. Several transmitter frequency offsets were tested to cover the large expected chemical shift range. In Figure S10, spectra are plotted with the same vertical scales (except for the $SnO_2$ data) to allow comparison of noise levels. The rotors for the $CsSn^{II}Br_3$ and $Cs_2Sn^{IV}Br_6$ each contained about 60 mg of sample, while that for the denser **1:Sn** contained 97 mg of sample.

Despite long total acquisition times for the sample of pulverized crystals of **1:Sn** (1 atom% Sn) of 25–33 h, no signals were detected above the noise. Clear, relatively broad (ca. 30 ppm FWHM) resonances were observed for shorter acquisitions for $CsSn^{II}Br_3$ at −370 ppm and $Cs_2Sn^{IV}Br_6$ at −1965 ppm.

**Solution-state NMR**

Samples of $Cs_2Sn^{IV}Br_6$, $CsSn^{II}Br_3$, and crystals of **1:Sn** (1 atom% Sn) were each dissolved in 1 g of DMSO-$d_6$. NMR data were collected on a 300 MHz Varian Inova NMR spectrometer (111.7 MHz for $^{119}Sn$) equipped with a broadband probe at 20°C. The $^{119}Sn$ NMR data were acquired with 134,456 points over 336,134 Hz with an acquisition time of 0.2 s and a recycle delay of 5 s, using a 45° excitation pulse of 4.5 μs. The data for $Cs_2Sn^{IV}Br_6$ were acquired with 11,468 scans for a total time of 16 h 35 min. The data for $CsSn^{II}Br_3$ were acquired with 1268 scans for a total time of 1 h 51 min. The data for **1:Sn** were acquired with 1256 scans for a total time of 18 h. The data were processed using MNova with a 1, 10, and 100 Hz line-broadening apodization function for $Cs_2Sn^{IV}Br_6$, $CsSn^{II}Br_3$, and **1:Sn**, respectively, referenced indirectly to $SnCl_4$ at −150 ppm.

**Optical spectroscopy**

*UV-vis diffuse reflectance spectroscopy.* UV-vis diffuse reflectance spectra of crystals and thin films were collected using a Cary 6000i spectrophotometer equipped with an integrating sphere in reflectance mode. UV-vis measurements were performed in ambient atmosphere. To minimize degradation, the samples were removed from inert atmosphere immediately prior to preparation and measurement. Crystals were adhered

to a glass slide with grease, which is transparent at energies below 3.0 eV. A glass slide covered with the same grease was used as a blank. For thin film samples, a glass slide was used as the blank. The samples were center-mounted in the integrating sphere and angled 10º off normal incidence to prevent significant specular reflection from exiting the sphere. UV-vis diffuse reflectance of ball-milled powders were obtained using a Shimadzu UV-2600 spectrophotometer equipped with an integrating sphere in reflectance mode. Powders were diluted in a mull with $BaSO_4$ by a factor of ~20, by mass, and pressed into a sample puck, which was mounted at the back of the integrating sphere. A sample puck filled with pure $BaSO_4$ was used as a blank. The obtained reflectance spectra of crystals and powders were converted to pseudo-absorbance spectra using the Kubelka-Munk transformation.[12, 13] The obtained reflectance spectra for thin films were converted to absorbance using the formula:

$$\text{Absorbance} = 2 - \log(\%R)$$

*UV-vis transmittance spectroscopy.* UV-vis transmittance spectra of thin films were collected using a Cary 6000i spectrophotometer in transmission mode. UV-vis measurements were performed in ambient atmosphere; to minimize degradation, the samples were removed from inert atmosphere immediately prior to measurement. A glass slide was used as the blank. The obtained transmittance spectra were converted to absorbance using the formula:

$$\text{Absorbance} = 2 - \log(\%T)$$

*Optical bandgap determination.* See Slavney *et al.*[13] for a detailed discussion of bandgap extraction from the UV-vis spectrum of **1**.

*Photothermal deflection spectroscopy (PDS).* PDS measurements were performed on a home-built setup described by Vandewal *et al.*[14] Measurements were taken using a mechanically chopped (2 Hz) monochromatic light source using both a 150 W Xenon and 100 W halogen pump lamp with 5 nm spectral resolution focused onto the sample. Degassed and filtered perflourohexane ($C_6F_{14}$, 3M Flourinert FC-72) was used as the deflection medium. Films of **1** and **1:Sn** were synthesized according to the spincoating procedure outlined above on quartz substrates. The samples were kept under inert atmosphere until the completion of the measurement. Each sample was aligned with maximal overlap between the pump beam and thin film. Samples were normalized for extinction above the bandgap using the procedure described by Buchaca-Domingo *et al.*[15] Urbach energies ($E_u$) were determined by plotting $\alpha$ on a natural log scale against photon energy ($E$) on a linear scale, making a linear fit to the low-energy region ($\alpha<10^4$), and taking the inverse of the slope of the linear fit according to the equation:

$$\ln(\alpha) = \ln(\alpha_0) + [(E - E_0)/E_u]$$

where $E_0$ and $\alpha_0$ are constants that are characteristic of the material.

**Atomic force microscopy (AFM)**

AFM imaging was performed using a Park XE-70 equipped with an NSC-15 tip operating in non-contact mode. Thin film samples were prepared on doped-Si substrates and did not require adherence to the sample stage for imaging stability. The sample chamber was under ambient conditions; to minimize degradation of the samples, the samples were removed from inert atmosphere immediately prior to beginning measurements.

**Electron microscopy**

Scanning electron microscopy images were collected using an FEI XL30 Sirion SEM and an FEI Magellan 400 XHR SEM. Thin film samples were synthesized on doped-Si substrates to minimize charging effects. Exposure of the samples to ambient atmosphere was limited to under 45 s during the sample mounting and loading process. Energy-dispersive X-ray spectroscopy (EDX) and concentric backscatter (CBS) data were collected using the FEI Magellan 400 XHR SEM equipped with an XFlash 6 | 60 SDD EDX detector. During EDX mapping, live secondary electron imaging was performed over the region of interest to minimize drift during pattern acquisition. EDX maps were acquired with an accelerating voltage of 20 kV and 6.4 nA total current and a detector distance of 8–10 mm. CBS images were acquired with an accelerating voltage of 10 kV and 0.8 nA total current and a detector distance of 8–10 mm.

**Elemental analysis**

Elemental analysis was performed by Huffman Hazen Laboratories (Golden, CO), by inductively coupled plasma (ICP) analysis. Crystal samples were digested in a mixture of nitric and perchloric acids and the concentrations of Ag and Bi were determined by atomic emission spectroscopy (ICP-AES) while the concentrations of Cs and Sn were determined by mass spectrometry (ICP-MS). Due to the low solubility of AgBr necessitating aggressive digestion methods that oxidize $Br^-$ to $Br_2$, the Br content in the sample could not be measured directly but was inferred from the sum of the other masses. Each sample was split into two portions and run in duplicate. The compositions of each sample are given in Table S1 and Figure S1. Three different samples of the 1 atom% Sn **1:Sn** crystals were each split into two separate parts and analyzed to assess reproducibility. One outlier was excluded, leaving five total measurements for the average elemental composition of the 1 atom% Sn **1:Sn** crystals.

**Computation**

Our density functional theory (DFT) calculations are performed using the generalized gradient approximation of Perdew, Burke, and Ernzerhof (PBE) and the projector augmented wave formalism (PAW) as implemented in VASP.[16, 17] The PAW potentials used here include 9 valence electrons for Cs ($5s^25p^66s^1$), 11 for Ag ($4d^{10}5s^1$), 5 for Bi ($6s^26p^3$), 4 for Sn ($5s^25p^2$), and 7 for Br ($4s^24p^5$). For 80 atom supercells of $Cs_2AgBiBr_6$ we perform Brillouin zone integrations on 4 × 4 × 4 Γ-centered *k*-point meshes, scaled proportionally for the larger unit cells, as well as a plane-wave cutoff of 500 eV, with spin-orbit coupling taken into account self-consistently. The structural relaxations are performed without SOC, allowing the internal coordinates and volume to relax until Hellmann-Feynman forces are less than 0.01 eV/Å. Calculated and experimental structural parameters can be found in Tables S4–S6.

Given the nominal charge of Sn is even and those of Ag and Bi are odd, substitution of Sn for either Ag or Bi without including charge-compensating vacancies is expected to lead to a metallic system due to an excess of electrons. Because of this, and because the experimental data suggest that the Ag and Bi sites have reduced occupation in **1:Sn** relative to **1**, we introduced vacancies in addition to the Sn substitutions. We tested different combinations of Sn substitutions and vacancies on Ag and/or Bi sites that would nominally result in a $Sn^{2+}$ or $Sn^{4+}$ oxidation state, assuming oxidation states of $Ag^+$ and $Bi^{3+}$. For $Sn^{2+}$, this can arise from Case 1: one Sn replacing one Ag and one vacancy replacing one Ag; Case 4: one Sn replacing one Ag and one Sn replacing one Bi (giving rise to two $Sn^{2+}$ sites). For $Sn^{4+}$, this can arise from Case 2: one Sn replacing one Bi and one vacancy replacing one Ag; Case 3: three Sn replacing three Bi and one vacancy replacing one Bi. In the latter scenario, the larger number of sites requires a larger supercell to maintain a

Sn concentration comparable to experiment, which becomes computationally prohibitive. In this case, we limit our work to a 160-atom supercell, corresponding to a Sn concentration of 1.875 atom%, slightly higher than that accessible in crystals of **1:Sn**, though lower than that accessible in films of **1:Sn**. Nonetheless, these calculations should still predict the hybridization of bands expected with this type of substitution of in a more dilute or more concentrated substitution. For each of these substitution cases, the total energies for each substitution of the Sn and vacancies on the different Ag and Bi sites in the supercells were compared. In all cases, the substitutions on adjacent sites are slightly energetically preferred (<100 meV), therefore, these configurations are used to report the calculated bandgaps. The calculated bandgap (calculated with DFT-PBE-SOC) can change by up to 0.14 eV based on the supercell configuration. However, comparison of the lowest- and highest-energy structures reveals that the general features of the band structures are similar, especially the orbital character of the bands at the band edges. We further compare the relative formation energies based on these total energies of the relaxed structures relative to the solid elemental compounds as $E_{formation} = \left(E_{alloyed} - E_{non-alloye}\right) + \sum_{\alpha} n_{\alpha}\mu_{\alpha}$, where α denotes the atomic species and $\mu_{\alpha}$ is the energy per atom for the respective elemental solids, with the results shown in Table S7.

In order to assess the effect of nominal mixed valence substitution, we constructed a 320-atom supercell of **1:Sn** and modeled it to mimic a 2:1 $Sn^{2+}$:$Sn^{4+}$ alloying concentration (see Table S8). Given the large number of atoms, we chose a representative substitution pattern based on the other calculations suggesting that the Sn and vacancies energetically prefer to substitute on adjacent sites rather than comparing the energies of all possible cases. The internal coordinates were relaxed without including SOC, after which the band structure was computed including SOC.

**Table S1.** Elemental analysis of crystals of **1:Sn** by ICP-MS/ICP-OES.

| Sample | $SnBr_2$ in solution as mol. eq. of $Cs_2AgBiBr_6$ | Atom% in solid | | | | |
|---|---|---|---|---|---|---|
| | | Cs[a] | Ag[b] | Bi[b] | Sn[a] | Br[c] |
| 1 | 0 | 19.6(1) | 9.44(2) | 9.5(1) | 0.0011(2) | 61.4(2) |
| 2 | 0.01 | 19.6(6) | 9.37(4) | 9.5(2) | 0.023(1) | 61.5(6) |
| 3 | 0.1 | 19.6(2) | 9.18(1) | 9.515(7) | 0.069(9) | 61.7(2) |
| 4 | 0.25 | 19.697(7) | 9.24(3) | 9.54(4) | 0.10(2) | 61.42(5) |
| 5 | 0.5 | 19.56(3) | 9.10(2) | 9.53(7) | 0.16(3) | 61.65(8) |
| 6 | 1 | 19.7(3) | 8.80(2) | 9.44(4) | 0.31(2) | 61.8(3) |
| 7[d] | 2 | 19.69(4) | 8.11(6) | 9.1(1) | 1.0(2) | 62.1(4) |

[a] Content determined by ICP-MS.
[b] Content determined by ICP-OES.
[c] Bromide and metal content could not be simultaneously determined. The missing mass in each sample was assumed to be due entirely to bromide, thus bromide content was determined by subtraction.
[d] Average of three separately synthesized samples each split into two separate parts. One outlier was excluded, leaving five total measurements for the average.

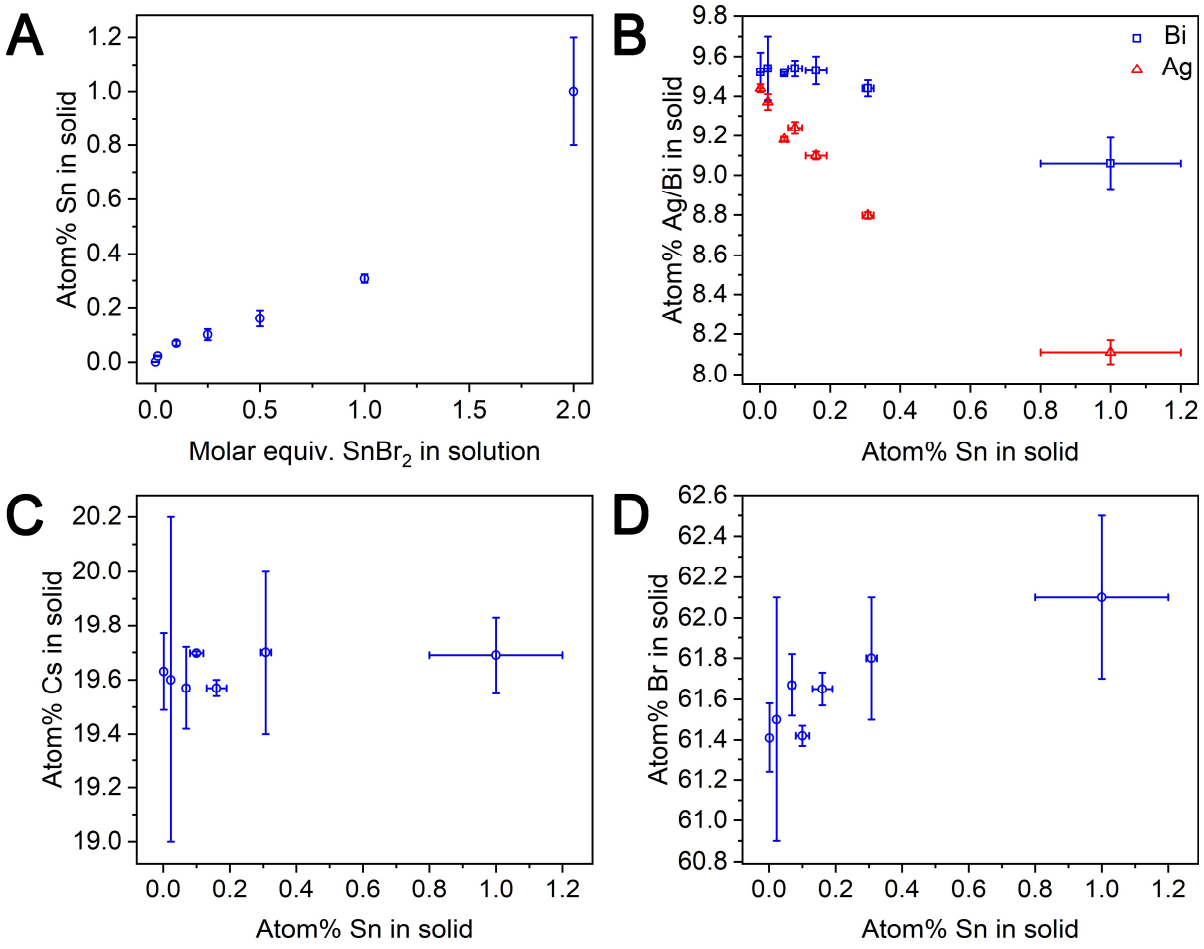


**Figure S1.** A) Concentration of Sn in crystals of **1:Sn** measured by ICP versus molar equivalents of $SnBr_2$ in the crystallization solution with respect to the concentration of **1** in the crystallization solution. B) Ag and Bi, C) Cs, and D) Br concentrations measured by ICP in crystals of **1:Sn** versus atom% Sn in the solid. Data from five samples were averaged for the 1 atom% Sn alloy. The Br content was calculated by subtraction (see text for details).

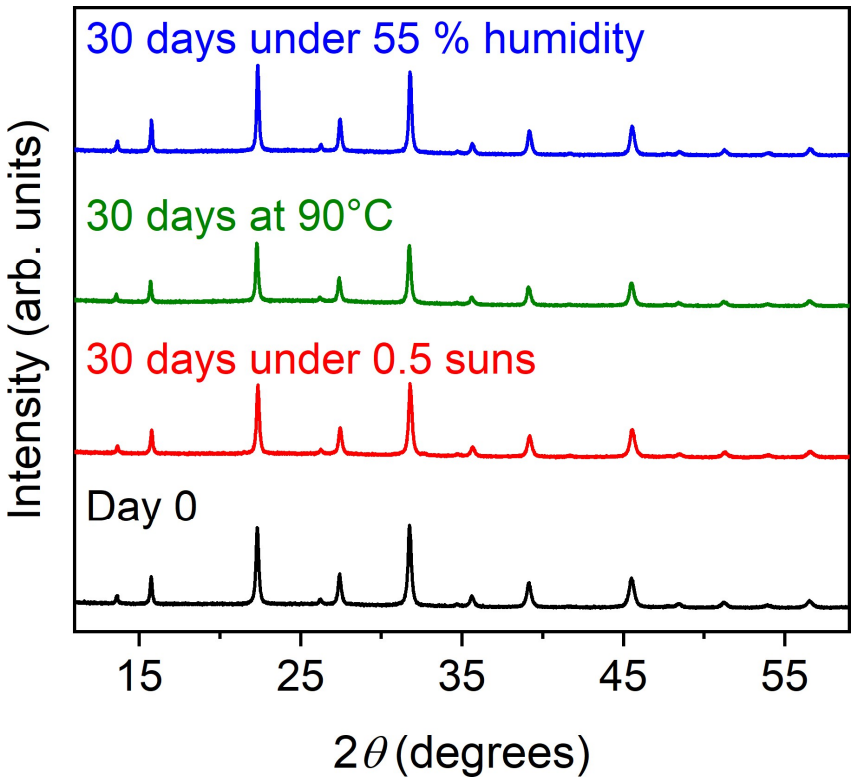


**Figure S2.** PXRD patterns of pulverized crystals of **1:Sn** (1 atom% Sn) exposed for 30 days to 0.5 suns under flowing $N_2$, heating at 90 ºC in ambient atmosphere, and exposed to 55% relative humidity in a jar sealed initially under ambient atmosphere.

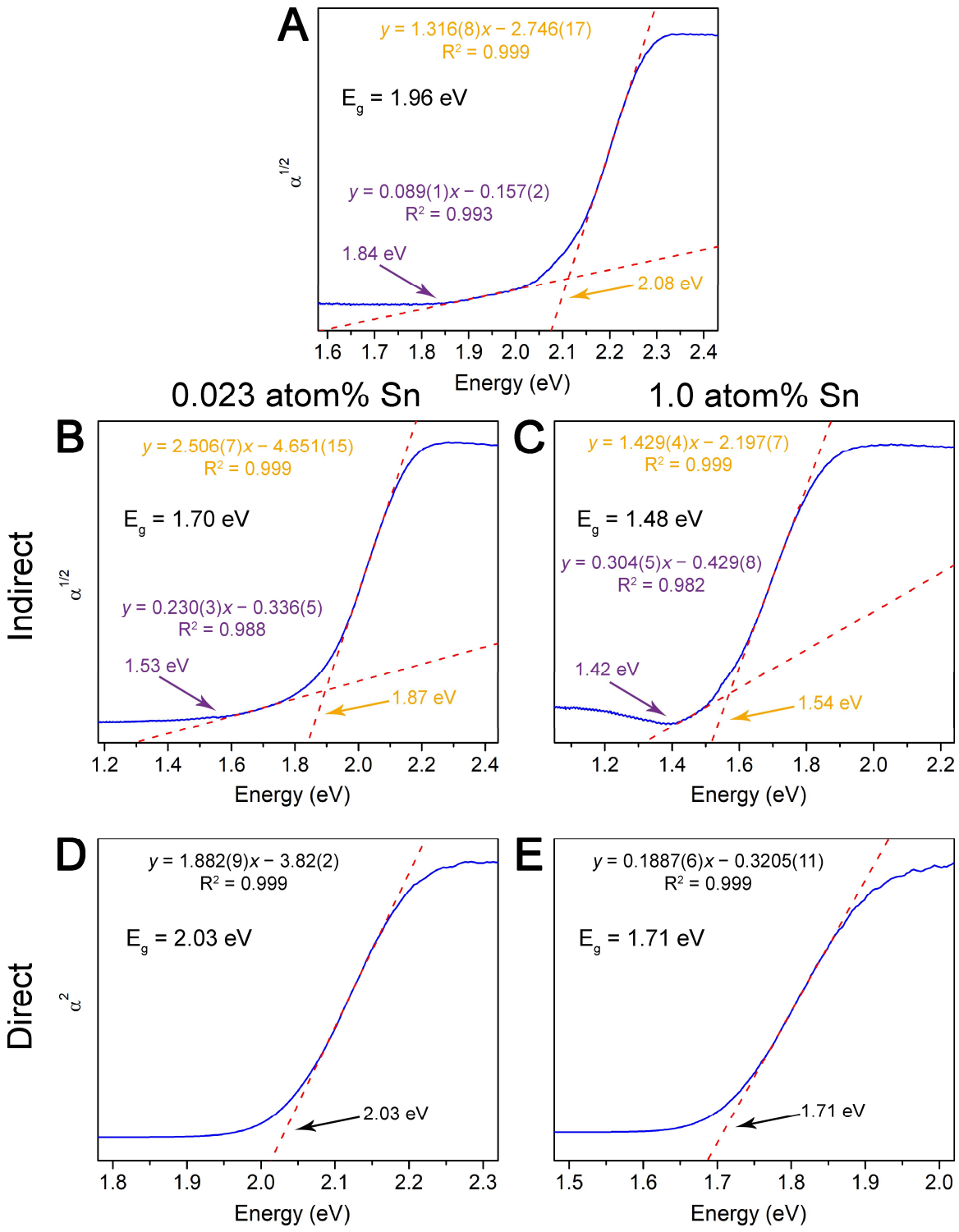


**Figure S3.** A) Plots of $\alpha^{1/2}$ versus $E$ extracted from UV-vis diffuse reflectance spectra of crystals of A) **1**, B) **1:Sn** (0.023 atom% Sn), and C) **1:Sn** (1.0 atom% Sn) for an assumed indirect bandgap, showing the linear fits. Plots of $\alpha^2$ vs. $E$ extracted from UV-vis diffuse reflectance spectra of crystals of D) **1:Sn** (0.023 atom% Sn) and E) **1:Sn** (1.0 atom% Sn) for an assumed direct bandgap, showing the linear fits.

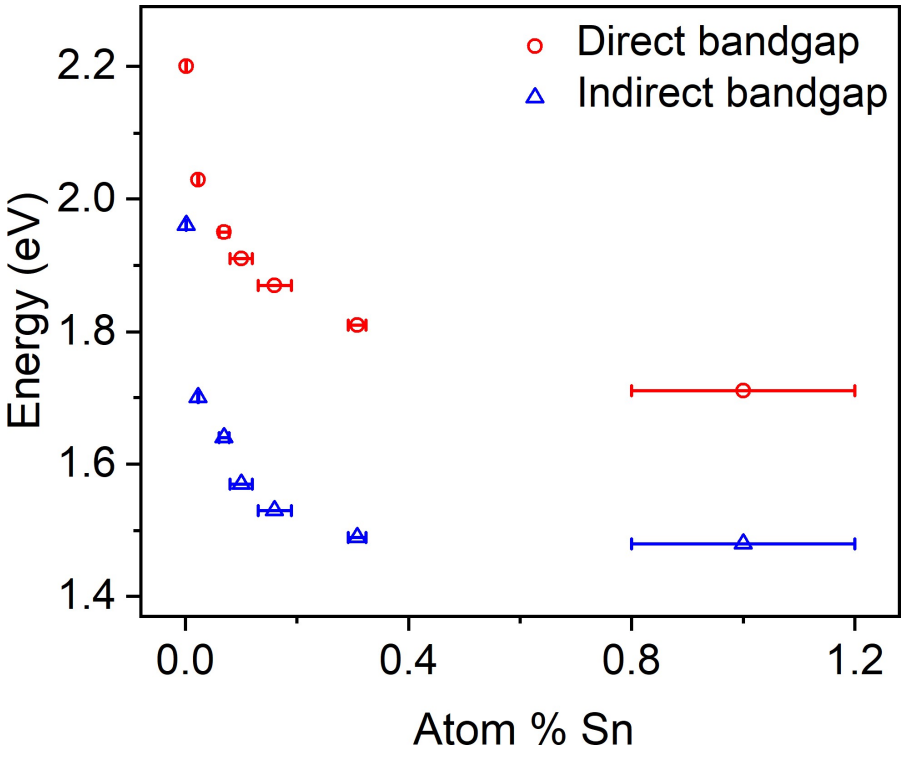


**Figure S4.** Dependence of the bandgap of crystals of **1:Sn** on the concentration of Sn. Bandgaps were extracted by linear fits to plots of $\alpha^2$ versus $E$ (direct bandgap) and $\alpha^{1/2}$ versus $E$ (indirect bandgap) (see Figure S3). Data from five samples were averaged for the 1 atom% Sn alloy.

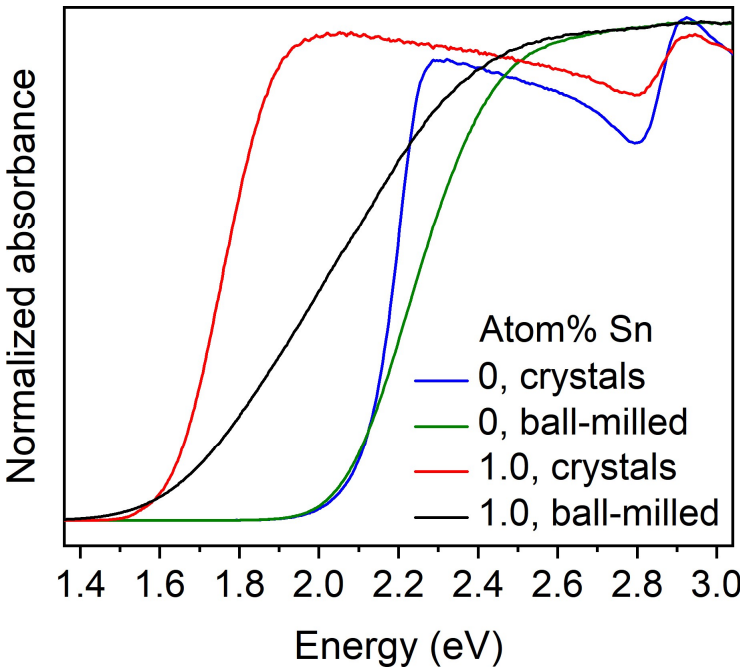


**Figure S5.** UV-vis absorbance spectra of crystals and ball-milled crystals of **1** and **1:Sn** converted from diffuse reflectance spectra using the Kubelka-Munk transformation. The absorption onsets appear independent of particle size.

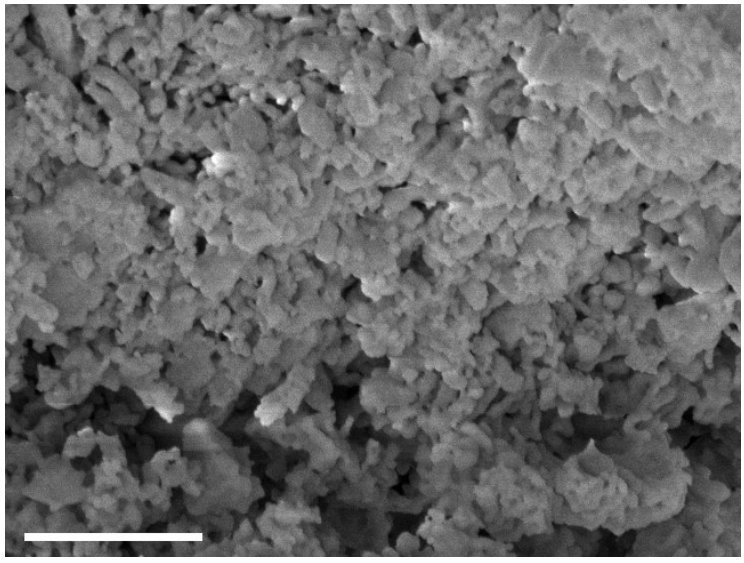

**Figure S6.** A representative SEM image of ball-milled crystals of **1:Sn** (1 atom% Sn). The scale bar is 2 μm.

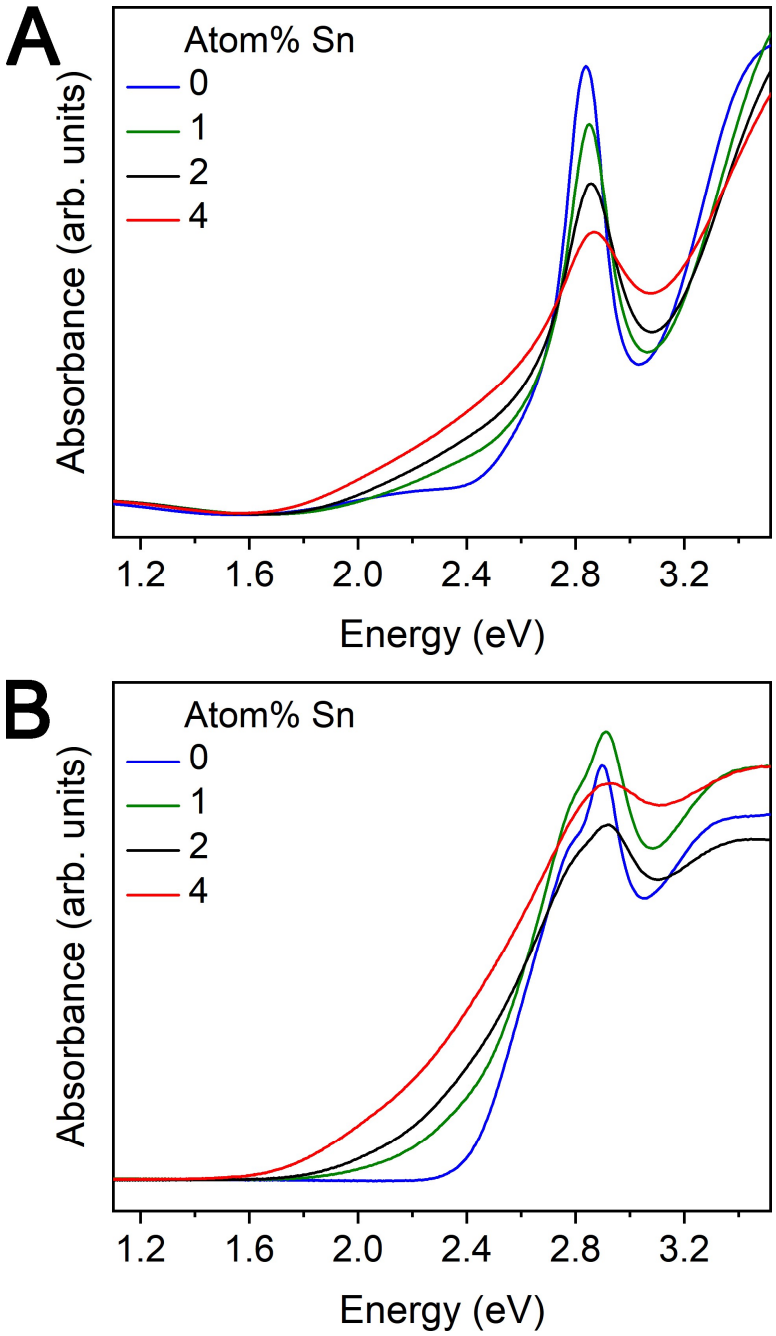


**Figure S7.** A) UV-vis transmission spectra of thin films of **1** and **1:Sn**. B) UV-vis absorbance spectra of the same samples shown in A) collected in an integrating sphere and converted from diffuse reflectance spectra via a logarithmic transformation (see text for details). The measurement taken in the integrating sphere confirms that the low-energy absorption is not due to scattering losses.

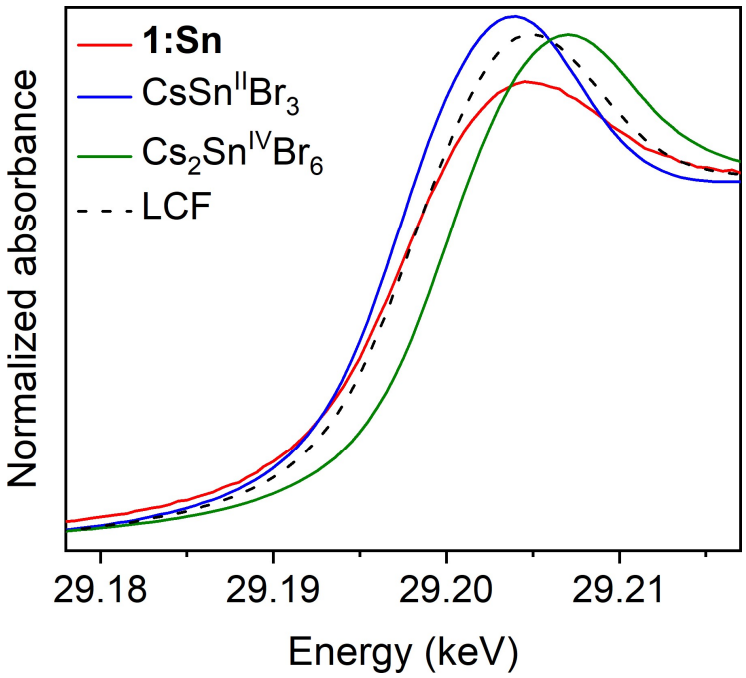


**Figure S8.** Sn K-edge XANES spectra of pulverized crystals of **1:Sn** (1 atom% Sn) and $CsSn^{II}Br_3$ and $Cs_2Sn^{IV}Br_6$ standards. LCF denotes a linear combination fit of the two standards' spectra to that of **1:Sn.**

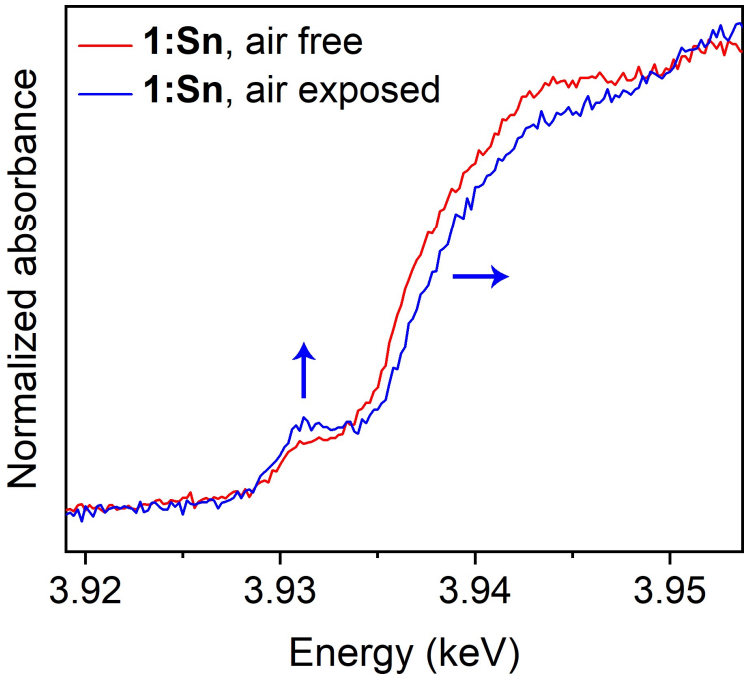


**Figure S9.** Sn $L_3$-edge XANES spectra of pulverized crystals of **1:Sn** (1 atom% Sn) before and after exposure to ambient atmosphere. The growth of the pre-edge feature and the blueshift of the edge indicate the oxidation of the $Sn^{2+}$.

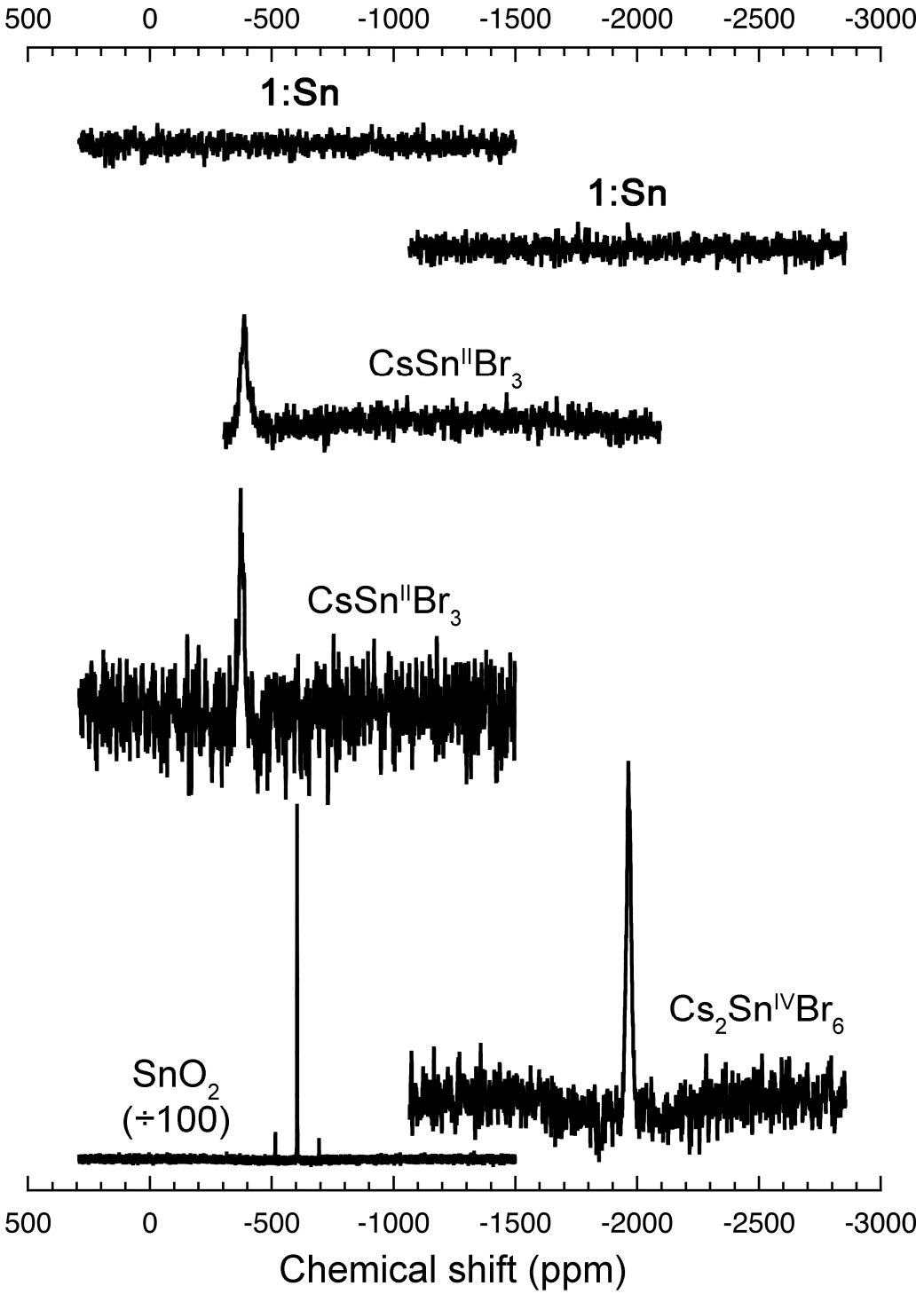


**Figure S10.** $^{119}$Sn magic-angle spinning solid-state NMR spectra of pulverized crystals of **1:Sn** (1 atom% Sn) and powders of $CsSn^{II}Br_3$, $Cs_2Sn^{IV}Br_6$, and $SnO_2$. Spectra of **1:Sn** and $CsSn^{II}Br_3$ were collected with two different frequency centers to cover a wider spectral range. All vertical scales are identical except for that of $SnO_2$, which is reduced by a factor of 100.

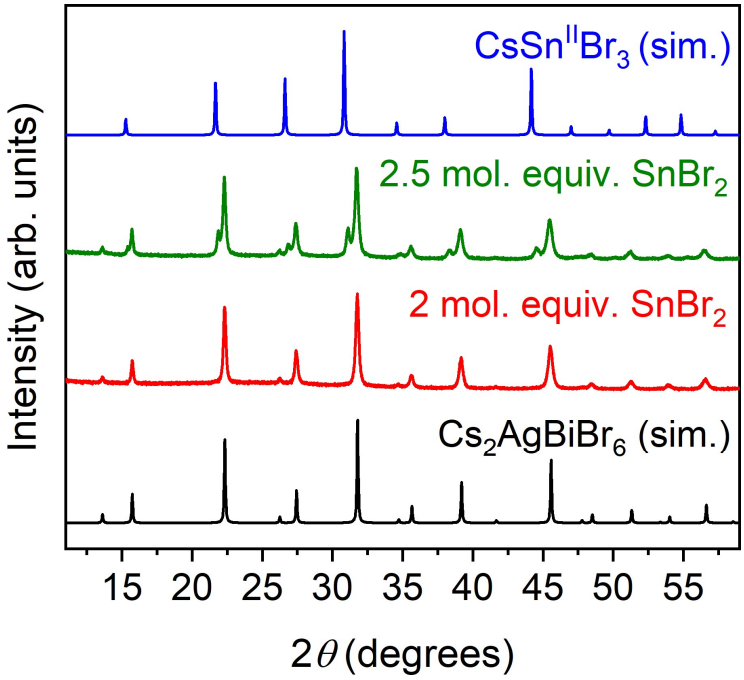


**Figure S11.** PXRD patterns of pulverized crystals of **1:Sn**. The Sn concentration in solution is given with respect to the concentration of **1** in solution.

**Table S2.** Crystallographic data for **1:Sn**.

| **Compound** | **1:Sn** (from phase-pure batch) | **1:Sn** (from phase-impure batch) |
|---|---|---|
| Empirical formula | $Cs_2Ag_{0.86}Sn_{0.07}BiBr_6$ | $Cs_2Ag_{0.65}Sn_{0.33}Bi_{0.85}Br_6$ |
| Formula weight (g/mol) | 1055.24 | 1031.32 |
| Temperature (K) | 300 | 300 |
| Crystal system | cubic | cubic |
| Space group | *Fm*-3*m* | *Fm*-3*m* |
| a, b, c (Å) | 11.2615(6) | 11.2749(11) |
| α, β, γ (°) | 90 | 90 |
| Volume ($Å^3$) | 1428.2(2) | 1433.3(4) |
| Z | 4 | 4 |
| Density, calc. ($g/cm^3$) | 4.907 | 4.779 |
| Absorption coeff. ($mm^{-1}$) | 32.509 | 33.512 |
| F(000) | 1787 | 1749 |
| Crystal size ($mm^3$) | 0.035 × 0.035 × 0.035 | 0.021 × 0.021 × 0.021 |
| Radiation | Synchrotron (λ = 0.68880 Å) | Mo-Kα (λ = 0.71073 Å) |
| 2$\theta$ range (°) | 3.036 to 27.239 | 3.129 to 25.311 |
| Index ranges | −14 ≤ h ≤ 14, −14 ≤ k ≤ 14, −14 ≤ l ≤ 14 | −13 ≤ h ≤ 13, −13 ≤ k ≤ 13, −13 ≤ l ≤ 13 |
| Reflections collected/unique | 11633/122 | 2929/96 |
| Completeness to $\theta_{max}$ | 1.000 | 1.000 |
| Max. and min. transmission | 0.3638, 0.3187 | 0.8129, 0.7120 |
| Independent reflections | $R_{int}$ = 0.0434 $R_{sigma}$ = 0.0101 | $R_{int}$ = 0.0516 $R_{sigma}$ = 0.0111 |
| Data/restraints/parameters | 122/1/10 | 95/1/11 |
| Goodness-of-fit on $F^2$ | 1.168 | 1.233 |
| Final R indexes [I>=2σ (I)] | $R_1$ = 0.0095, w$R_2$ = 0.0226 | $R_1$ = 0.0178, w$R_2$ = 0.0358 |
| Final R indexes [all data][a] | $R_1$ = 0.0095, w$R_2$ = 0.0226 | $R_1$ = 0.0186, w$R_2$ = 0.0362 |
| Largest diff. peak/hole ($e/Å^3$) | 0.313/−0.316 | 0.793/−0.578 |

[a] $R_1 = \Sigma||F_o| - |F_c||/\Sigma|F_o|$, $wR_2 = [\Sigma w(F_o^2 - F_c^2)^2/\Sigma(F_o^2)^2]^{1/2}$

**Table S3.** Predictions of Ag and Bi content of **1:Sn** using the experimentally determined Sn content (through ICP) with a ratio of 2:1 $Sn^{2+}$ to $Sn^{4+}$ and various substitution sites. "Vac" represents a vacancy. The values of Bi and Ag measured by ICP for **1** were used as the non-alloyed concentrations of Bi and Ag.

| Sample | Experimental atom% | | | $Sn^{2+}$ @ $Ag^{+}$ → $Ag^{+}$ vac; $Sn^{4+}$ @ $Bi^{3+}$ → $Ag^{+}$ vac | | $Sn^{2+}$ @ $Ag^{+}$ → $Ag^{+}$ vac; $3Sn^{4+}$ @ $Bi^{3+}$ → $Bi^{3+}$ vac | |
|---|---|---|---|---|---|---|---|
| | Sn | Ag | Bi | Pred. Ag atom% | Pred. Bi atom% | Pred. Ag atom% | Pred. Bi atom% |
| 1 | 0.0011(2) | 9.44(2) | 9.5(1) | 9.44 | 9.5 | 9.44 | 9.5 |
| 2 | 0.023(1) | 9.37(4) | 9.5(2) | 9.40 | 9.49 | 9.41 | 9.49 |
| 3 | 0.069(9) | 9.18(1) | 9.515(7) | 9.33 | 9.48 | 9.35 | 9.47 |
| 4 | 0.10(2) | 9.24(3) | 9.54(4) | 9.27 | 9.47 | 9.31 | 9.46 |
| 5 | 0.16(3) | 9.10(2) | 9.53(7) | 9.17 | 9.45 | 9.23 | 9.43 |
| 6 | 0.31(2) | 8.80(2) | 9.44(4) | 8.92 | 9.40 | 9.03 | 9.36 |
| 7 | 1.0(2) | 8.11(6) | 9.1(1) | 7.77 | 9.17 | 8.11 | 9.06 |

| $Sn^{2+}$ @ $Ag^{+}$ → $Ag^{+}$ vac; $Sn^{4+}$ @ $Ag^{+}$ → $3Ag^{+}$ vac | | $2Sn^{2+}$ @ 50/50 $Ag^{+}/Bi^{3+}$ → no vac; $Sn^{4+}$ @ $Bi^{3+}$ → $Ag^{+}$ vac | | $2Sn^{2+}$ @ 50/50 $Ag^{+}/Bi^{3+}$ → no vac; $2Sn^{4+}$ @ 50/50 $Ag^{+}/Bi^{3+}$ → $4Ag^{+}$ vac | | $Sn^{2+}$ @ $Ag^{+}$ → $Ag^{+}$ vac; no $Sn^{4+}$ | |
|---|---|---|---|---|---|---|---|
| Pred. Ag atom% | Pred. Bi atom% | Pred. Ag atom% | Pred. Bi atom% | Pred. Ag atom% | Pred. Bi atom% | Pred. Ag atom% | Pred. Bi atom% |
| 9.44 | 9.5 | 9.44 | 9.5 | 9.44 | 9.5 | 9.44 | 9.5 |
| 9.38 | 9.5 | 9.42 | 9.48 | 9.41 | 9.49 | 9.39 | 9.5 |
| 9.26 | 9.5 | 9.39 | 9.45 | 9.36 | 9.47 | 9.30 | 9.5 |
| 9.17 | 9.5 | 9.37 | 9.43 | 9.32 | 9.45 | 9.24 | 9.5 |
| 9.01 | 9.5 | 9.33 | 9.39 | 9.25 | 9.42 | 9.12 | 9.5 |
| 8.61 | 9.5 | 9.23 | 9.29 | 9.08 | 9.35 | 8.82 | 9.5 |
| 6.77 | 9.5 | 8.77 | 8.83 | 8.27 | 9.00 | 7.44 | 9.5 |

**Table S4.** The spatial locations of the Sn atom(s) and/or vacancy and total energy of the relaxed structure computed with DFT-PBE in a 2 × 1 × 1 supercell (lattice parameters $a$ = 22.50 Å, $b = c$ = 11.25 Å), calculated for various substitution patterns. The qualitative features of orbital hybridization in the electronic band structures are insensitive to the configuration. "Vac" represents a vacancy.

| $Sn^{2+}$ @ $Ag^{+}$ → $Ag^{+}$ vac | | |
|---|---|---|
| Coordinates of Sn | Coordinates of vacancy | Energy relative to lowest-energy configuration (meV) |
| (0.0, 0.0, 0.5) | (0.5, 0.0, 0.0) | 14.2 |
| (0.0, 0.0, 0.5) | (0.0, 0.5, 0.5) | 0.0 |
| (0.0, 0.0, 0.5) | (0.5, 0.5, 0.5) | 42.8 |
| (0.0, 0.0, 0.5) | (0.25, 0.0, 0.5) | 17.4 |
| (0.0, 0.0, 0.5) | (0.75, 0.0, 0.5) | 17.2 |
| (0.0, 0.0, 0.5) | (0.25, 0.5, 0.0) | 16.1 |
| (0.0, 0.0, 0.5) | (0.75, 0.5, 0.0) | 19.3 |

| $Sn^{4+}$ @ $Bi^{3+}$ → $Ag^{+}$ vac | | |
|---|---|---|
| Coordinates of Sn | Coordinates of vacancy | Energy relative to lowest-energy configuration (meV) |
| (0.0, 0.0, 0.5) | (0.0, 0.0, 0.0) | 0.0 |
| (0.0, 0.0, 0.5) | (0.5, 0.0, 0.0) | 140.6 |
| (0.0, 0.0, 0.5) | (0.0, 0.5, 0.0) | 0.3 |
| (0.0, 0.0, 0.5) | (0.5, 0.5, 0.5) | 139.7 |
| (0.0, 0.0, 0.5) | (0.25, 0.0, 0.5) | 111.6 |
| (0.0, 0.0, 0.5) | (0.75, 0.0, 0.5) | 110.0 |
| (0.0, 0.0, 0.5) | (0.25, 0.5, 0.0) | 157.1 |
| (0.0, 0.0, 0.5) | (0.75, 0.5, 0.0) | 157.2 |

| $2Sn^{2+}$ @ 50/50 $Ag^{+}/Bi^{3+}$ | | |
|---|---|---|
| Coordinates of Sn @ $Ag^{+}$ | Coordinates of Sn @ $Bi^{3+}$ | Energy relative to lowest-energy configuration (meV) |
| (0.0, 0.0, 0.0) | (0.0, 0.5, 0.0) | 0.0 |
| (0.0, 0.0, 0.0) | (0.25, 0.5, 0.5) | 79.3 |
| (0.0, 0.0, 0.0) | (0.5, 0.0, 0.5) | 135.9 |
| (0.0, 0.0, 0.0) | (0.75, 0.0, 0.0) | 29.3 |
| (0.0, 0.0, 0.0) | (0.75, 0.5, 0.5) | 80.3 |

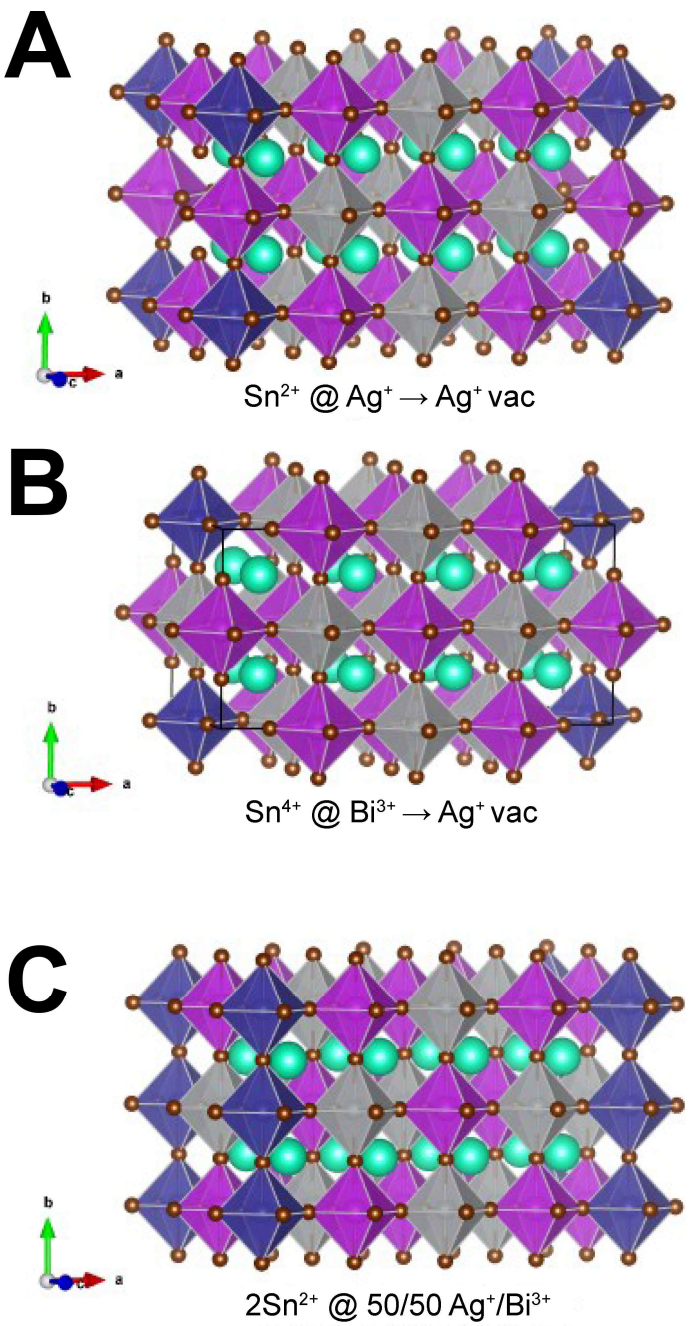


**Figure S12.** Representations of the lowest-energy structures of the supercells of **1:Sn** detailed in Table S4. The Cs atoms are shown in turquoise, Ag in grey, Bi in purple, Sn in dark blue, and Br in brown.

**Table S5.** The spatial locations of the Sn atoms and vacancies and total energy of the relaxed structure computed with DFT-PBE in a 2 × 2 × 1 supercell (lattice parameters $a = b = 22.50$ Å, $c = 11.25$ Å) for nominal substitution of $Sn^{4+}$ at the $Bi^{3+}$ site generating $Bi^{3+}$ vacancies. The qualitative features of orbital hybridization in the electronic band structures are insensitive to the configuration. "Vac" represents a vacancy.

| $3Sn^{4+}$ @ $3Bi^{3+}$ → $Bi^{3+}$ vac | | | | |
|---|---|---|---|---|
| Coordinates of vacancy | Coordinates of Sn 1 | Coordinates of Sn 2 | Coordinates of Sn 3 | Energy relative to lowest-energy configuration (meV) |
| (0.0, 0.0, 0.0) | (0.25, 0.0, 0.0) | (0.0, 0.25, 0.0) | (0.0, 0.0, 0.5) | 1.3 |
| (0.0, 0.0, 0.0) | (0.25, 0.25, 0.5) | (0.25, 0.0, 0.0) | (0.0, 0.25, 0.0) | 0.5 |
| (0.0, 0.0, 0.0) | (0.25, 0.25, 0.5) | (0.0, 0.25, 0.0) | (0.0, 0.0, 0.5) | 2.4 |
| (0.0, 0.0, 0.0) | (0.25, 0.25, 0.5) | (0.25, 0.0, 0.0) | (0.0, 0.0, 0.5) | 0.0 |
| (0.0, 0.0, 0.0) | (0.0, 0.5, 0.5) | (0.5, 0.0, 0.5) | (0.5, 0.5, 0.5) | 324.7 |
| (0.0, 0.0, 0.0) | (0.0, 0.0, 0.5) | (0.5, 0.0, 0.5) | (0.5, 0.5, 0.5) | 326.0 |
| (0.0, 0.0, 0.0) | (0.0, 0.0, 0.5) | (0.0, 0.5, 0.5) | (0.5, 0.5, 0.5) | 323.9 |
| (0.0, 0.0, 0.0) | (0.0, 0.0, 0.5) | (0.0, 0.5, 0.5) | (0.5, 0.0, 0.5) | 328.5 |

**Table S6.** The unit-cell parameters of **1** and **1:Sn** after relaxation with DFT-PBE for various substitutional cases. The conventional cell was used for **1**. All unit cell angles are 90º. "Vac" represents a vacancy.

| Substitution | Total Sn concentration (atom%) | Formula | Unit cell parameters (Å) |
|---|---|---|---|
| None | 0 | $Cs_2AgBiBr_6$ | $a = b = c = 11.46$ |
| $Sn^{2+}$ @ $Ag^+$ → $Ag^+$ vac | 1.25 | $Cs_2Ag_{0.75}Sn^{II}_{0.125}BiBr_6$ | $a = 22.98$<br>$b = c = 11.53$ |
| $Sn^{4+}$ @ $Bi^{3+}$ → $Ag^+$ vac | 1.25 | $Cs_2Ag_{0.875}Bi_{0.875}Sn^{IV}_{0.125}Br_6$ | $a = 22.87$<br>$b = 11.46$<br>$c = 11.44$ |
| $3Sn^{4+}$ @ $3Bi^{3+}$ → $Bi^{3+}$ vac | 1.875 | $Cs_2AgBi_{0.75}Sn^{IV}_{0.1875}Br_6$ | $a = b = 22.90$<br>$c = 11.45$ |
| $2Sn^{2+}$ @ 50/50 $Ag^+/Bi^{3+}$ | 2.5 | $Cs_2Ag_{0.875}Sn^{II}_{0.25}Bi_{0.875}Br_6$ | $a = 22.98$<br>$b = 11.57$<br>$c = 11.50$ |

**Table S7.** The relative formation energies for the Sn-alloyed structures calculated based on $E_{formation} = \left(E_{alloyed} - E_{non-alloye}\right) + \sum_{\alpha} n_{\alpha}\mu_{\alpha}$ where $\alpha$ denotes the atomic species and $\mu_{\alpha}$ is the energy per atom for the respective elemental solids.

| Substitution | Total energy per atom (eV) | Energy relative to **1** (eV) |
|---|---|---|
| none | –3.405 | 0 |
| $Sn^{2+}$ @ $Ag^{+} \rightarrow Ag^{+}$ vac | –3.437 | 1.654 |
| $Sn^{4+}$ @ $Bi^{3+} \rightarrow Ag^{+}$ vac | –3.405 | 2.721 |
| $2Sn^{2+}$ @ 50/50 $Ag^{+}/Bi^{3+}$ | –3.423 | –1.289 |

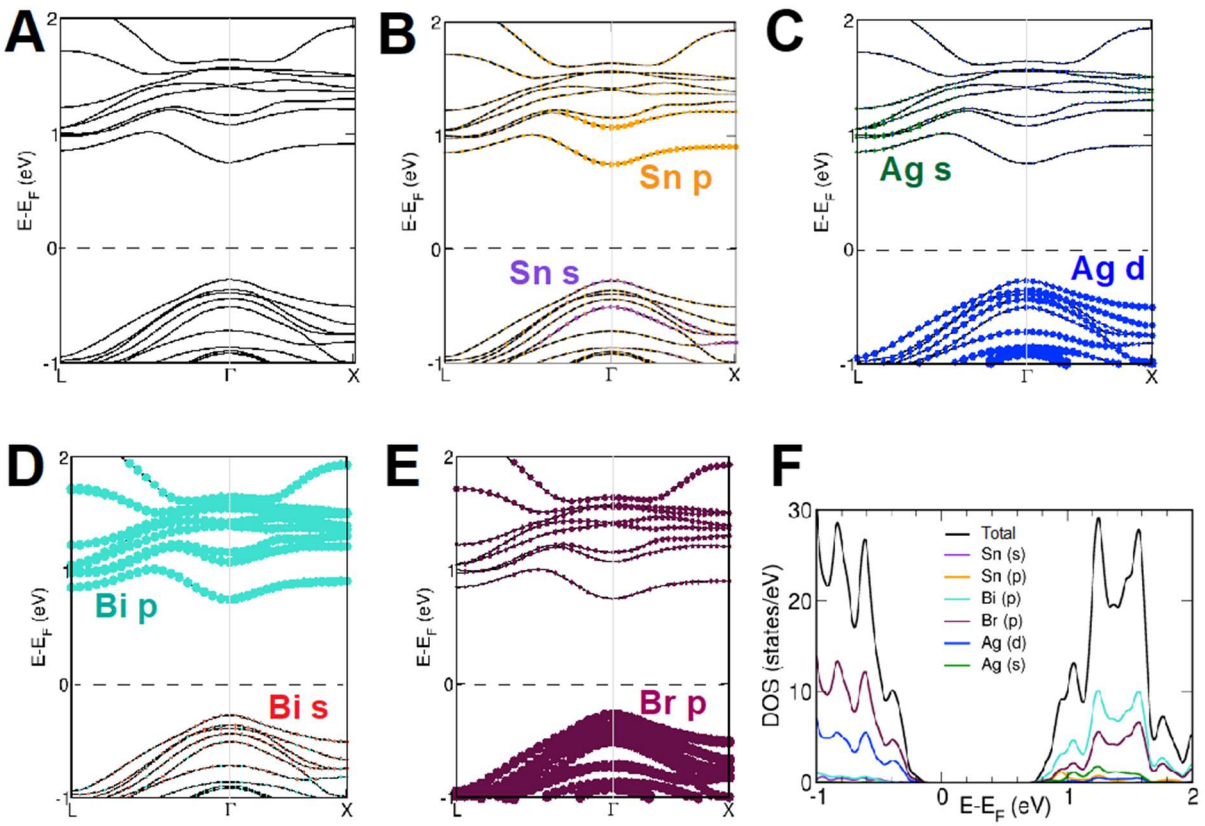


**Figure S13.** DFT-PBE-SOC band structure of **1:Sn** (1.25 atom% Sn) with two Ag atoms removed and replaced with one Sn and one vacancy, nominally resulting in a $Sn^{2+}$ oxidation state. The bandgap at the DFT-PBE-SOC level is computed to be 1.02 eV. Projections of the orbital character of the bands are shown in color in A–E), with the projected density of states in F). Here, $E_F$ indicates the Fermi energy.

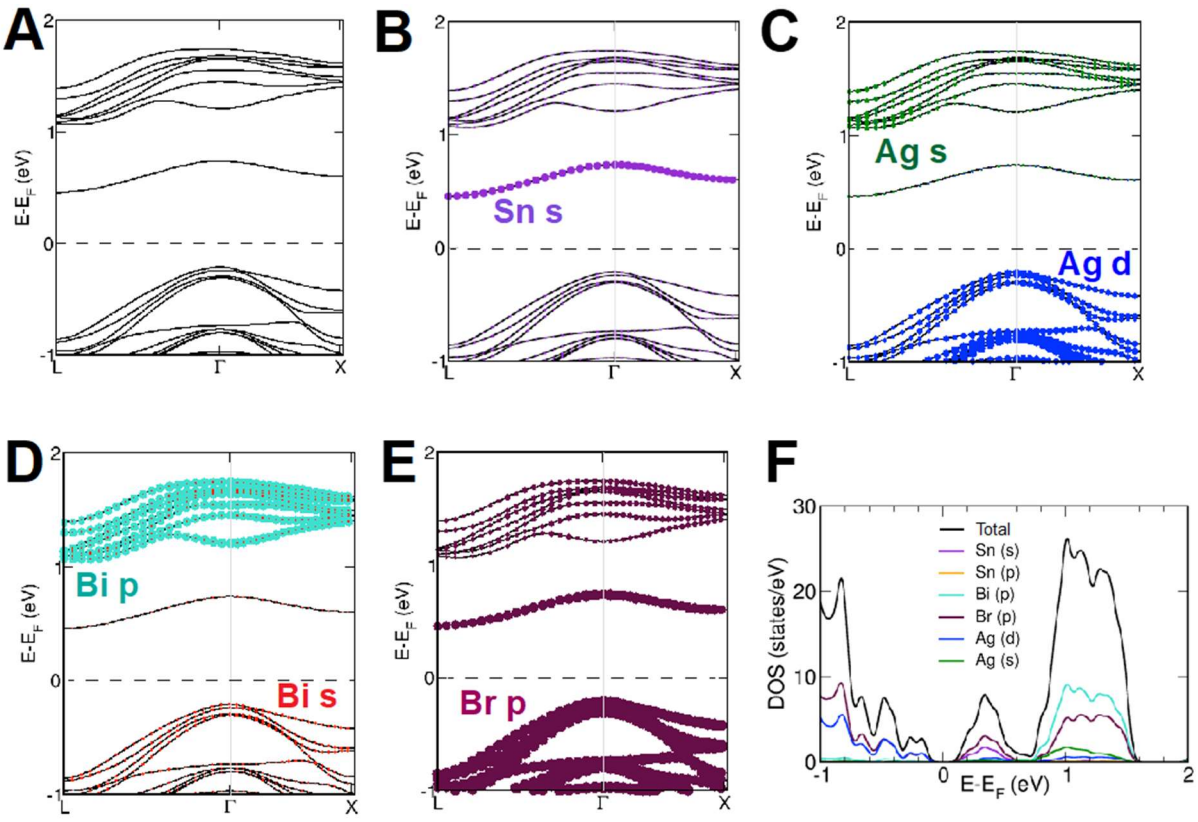


**Figure S14.** DFT-PBE-SOC band structure of **1:Sn** (1.25 atom% Sn) with one Ag atom replaced by a vacancy and one Bi atom replaced by Sn, nominally resulting in a $Sn^{4+}$ oxidation state. The bandgap at the DFT-PBE-SOC level is computed to be 0.67 eV. Projections of the orbital character of the bands are shown in color in A–E), with the projected density of states in F). Here, $E_F$ indicates the Fermi energy.

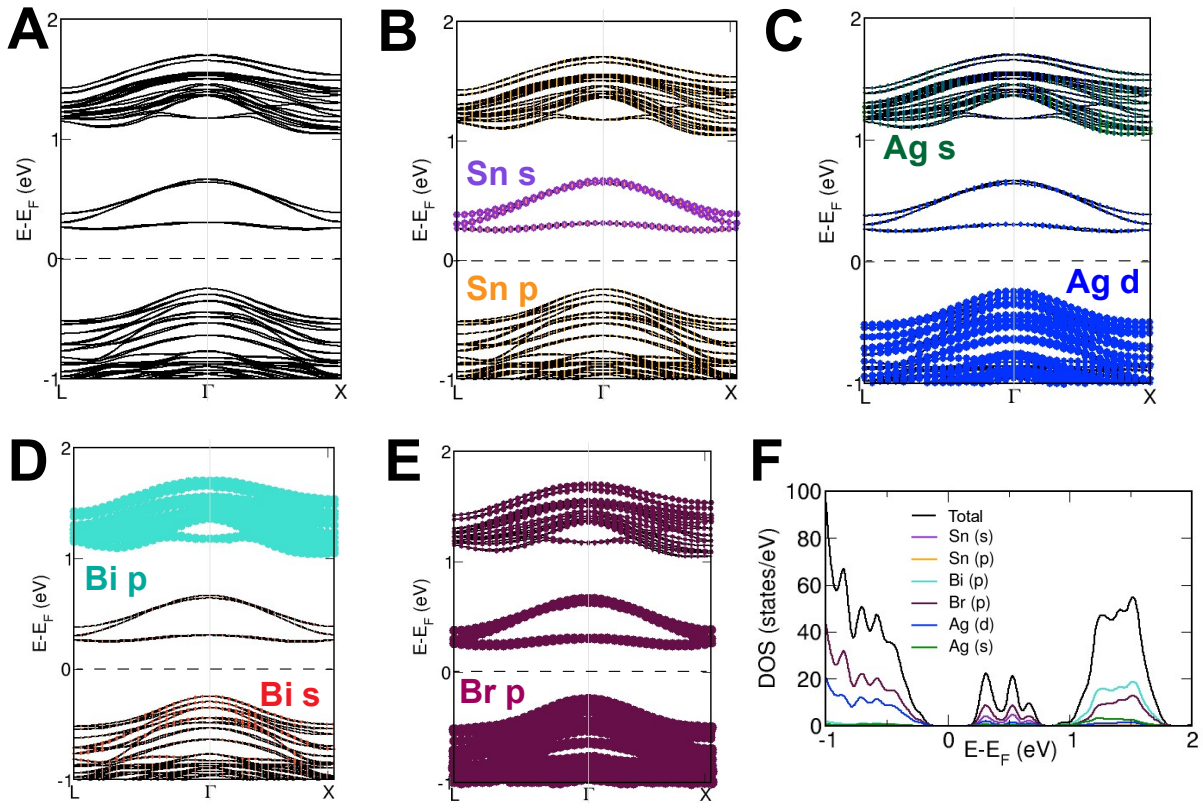


**Figure S15.** DFT-PBE-SOC band structure of **1:Sn** (1.875 atom% Sn) with four Bi atoms replaced by one vacancy and three Sn atoms, nominally resulting in a $Sn^{4+}$ oxidation state. The bandgap at the DFT-PBE-SOC level is computed to be 0.49 eV. Projections of the orbital character of the bands are shown in color in A–E), with the projected density of states in F). Here $E_F$ indicates the Fermi energy.

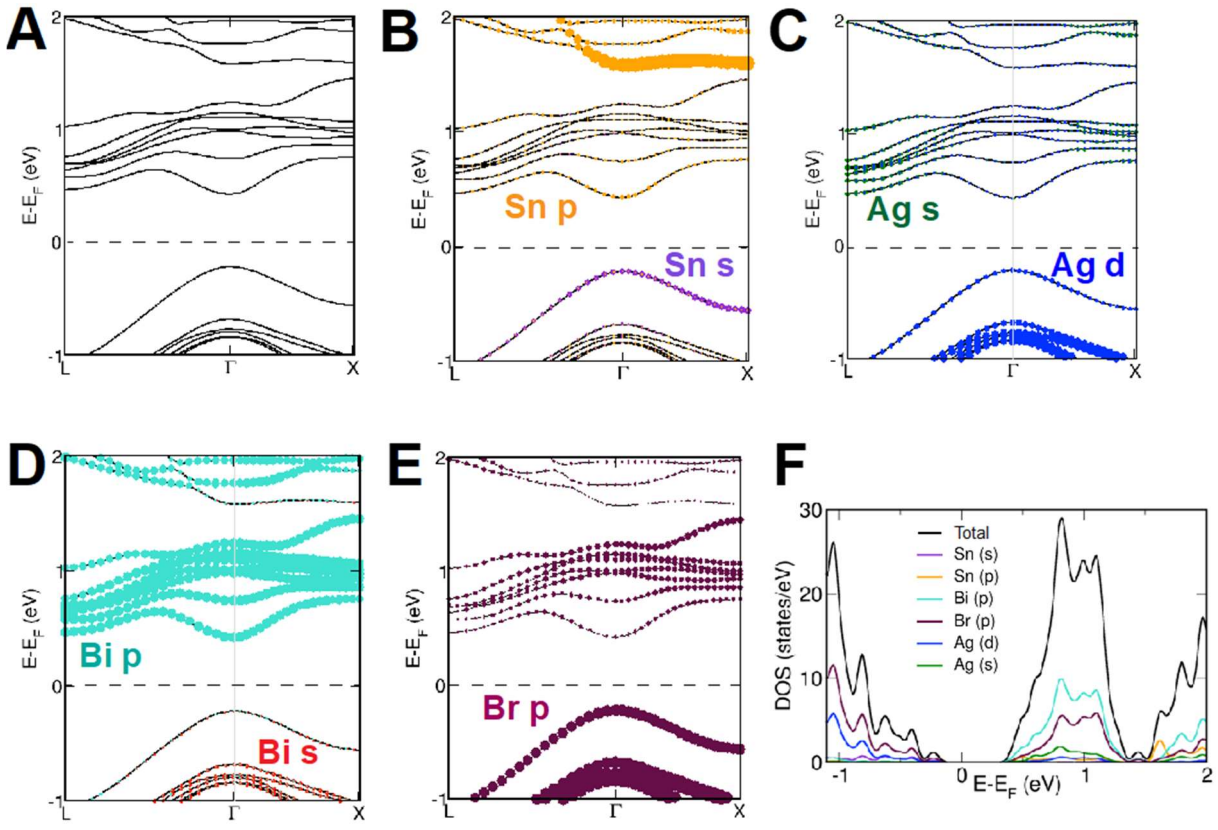


**Figure S16.** DFT-PBE-SOC band structure of **1:Sn** (2.5 atom% Sn) with one Ag and one Bi atom each replaced by an Sn atom, nominally resulting in a $Sn^{2+}$ oxidation state. The bandgap at the DFT-PBE-SOC level is computed to be 0.64 eV. Projections of the orbital character of the bands are shown in color in A–E), with the projected density of states in F). Here $E_F$ indicates the Fermi energy.

**Table S8.** The various substitution patterns in **1:Sn** for which band structures have been calculated. "Vac" indicates a vacancy. The metallic states are an artifact of the DFT bandgap underestimation (see Section 5 in main text).

| Substitution | Total Sn concentration (atom%) | Formula | Calculated bandgap |
|---|---|---|---|
| None | 0 | $Cs_2AgBiBr_6$ | 1.11 eV Indirect (experiment = 1.95 eV; indirect) |
| $Sn^{2+}$ @ $Ag^+$ → $Ag^+$ vac | 0.625 | $Cs_2Ag_{0.875}Sn^{II}_{0.0625}BiBr_6$ | 1.07 eV Direct |
| $Sn^{2+}$ @ $Ag^+$ → $Ag^+$ vac | 1.25 | $Cs_2Ag_{0.75}Sn^{II}_{0.125}BiBr_6$ | 1.02 eV Direct |
| $Sn^{2+}$ @ $Ag^+$ → $Ag^+$ vac | 2.5 | $Cs_2Ag_{0.5}Sn^{II}_{0.25}BiBr_6$ | 0.10 eV Indirect |
| $Sn^{2+}$ @ $Ag^+$ → $Ag^+$ vac | 5 | $Cs_2Sn^{II}_{0.5}BiBr_6$ | 1.46 eV Indirect |
| $Sn^{4+}$ @ $Bi^{3+}$ → $Ag^+$ vac | 1.25 | $Cs_2Ag_{0.875}Bi_{0.875}Sn^{IV}_{0.125}Br_6$ | 0.67 eV Indirect |
| $3Sn^{4+}$ @ $3Bi^{3+}$ → $Bi^{3+}$ vac | 1.875 | $Cs_2AgBi_{0.75}Sn^{IV}_{0.1875}Br_6$ | 0.49 eV Indirect |
| $2Sn^{2+}$ @ 50/50 $Ag^+/Bi^{3+}$ | 2.5 | $Cs_2Ag_{0.875}Sn^{II}_{0.25}Bi_{0.875}Br_6$ | 0.64 eV Direct |
| $2Sn^{2+}$ @ 50/50 $Ag^+/Bi^{3+}$ | 20 | $Cs_2Sn^{II}Br_3$ | 0.29 eV Direct |
| $Sn^{4+}$ @ $Bi^{3+}$ → $Ag^+$ vac | 10 | $Cs_2Sn^{IV}Br_6$ | 1.41 eV Direct |
| $Sn^{2+}$ @ $Ag^+$ → no vac | 1.25 | $Cs_2Ag_{0.875}Sn^{II}_{0.125}BiBr_6$ | Metallic |
| $Sn^{4+}$ @ $Ag^+$ → $3Ag^+$ vac | 1.25 | $Cs_2Ag_{0.5}BiSn^{IV}_{0.125}Br_6$ | Metallic |

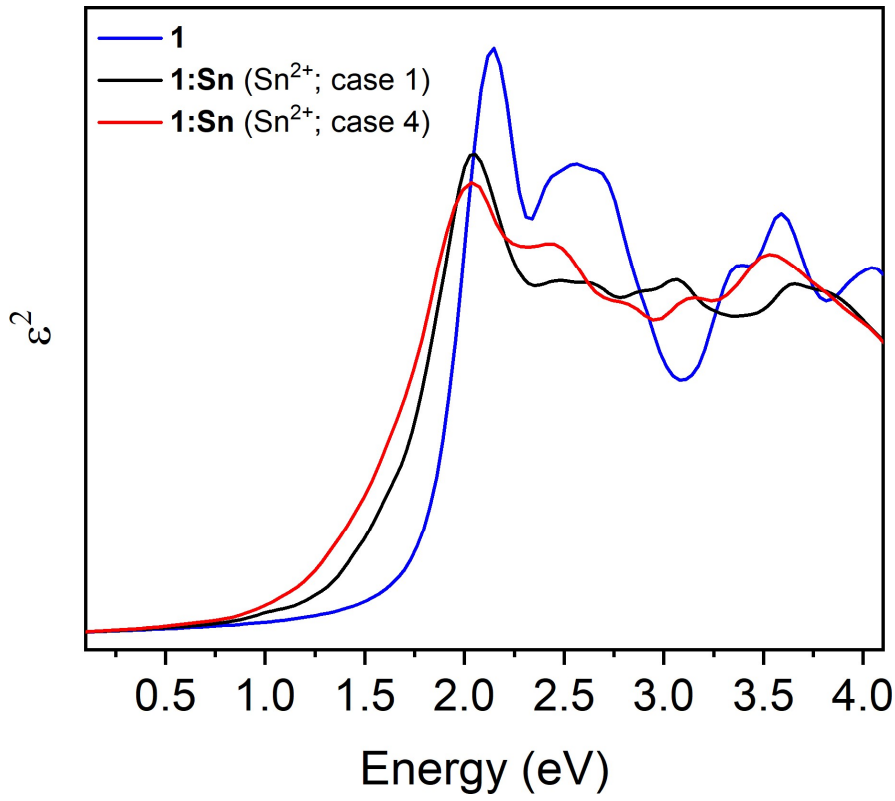


**Figure S17.** The imaginary part of the dielectric function as a function of energy as computed within the independent particle approximation. The results for **1** and for and two substitution patterns in **1:Sn** are computed, showing a decrease in the energy of the onset with Sn alloying.

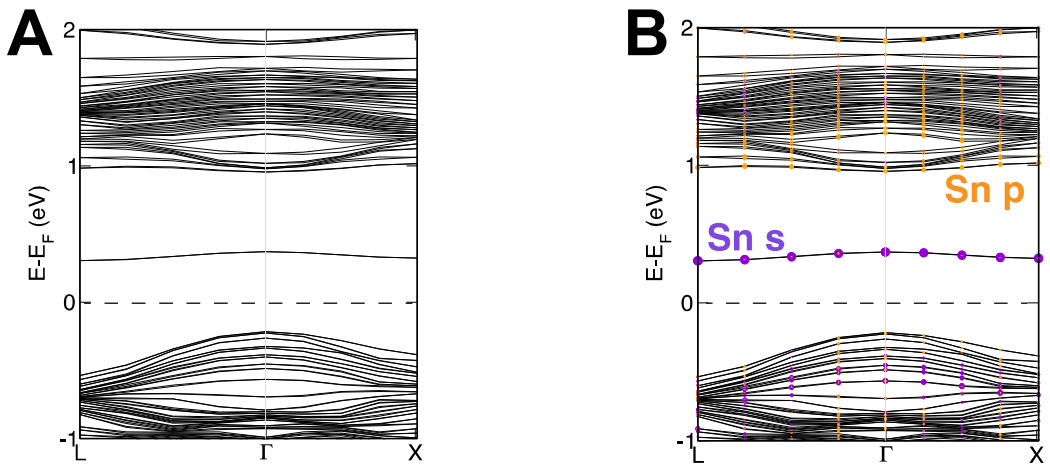


**Figure S18.** DFT-PBE-SOC band structure of **1:Sn** with two Ag and one Bi atom each replaced by Sn atoms and three Ag atoms replaced by vacancies, nominally resulting in a 2:1 ratio of $Sn^{2+}$: $Sn^{4+}$ in a 320-atom unit cell of **1**. The bandgap at the DFT-PBE-SOC level is computed to be 0.52 eV between the valence band maximum at Γ and the conduction band minimum at L. Projections of the Sn s and p character of the bands are shown in color in B). Here, $E_F$ indicates the Fermi energy. Note that due to the computational expense, a coarser *k*-grid density was used with 5 *k*-points computed along each of the high symmetry directions.

**Table S9.** The spatial locations of the Sn atoms and vacancies for the mixed-valence substitution case computed with DFT-PBE in a 2 × 2 × 2 supercell (lattice parameters $a = b = c = 22.50$ Å, ) for nominal substitution of 2:1 $Sn^{2+}$:$Sn^{4+}$. Two Ag atoms are replaced by Sn atoms and two other Ag atoms are replaced by vacancies to nominally model a two-$Sn^{2+}$-atom substitution; one Bi atom is replaced by an Sn atom and one other Ag atom is replaced by a vacancy to model a one-$Sn^{4+}$-atom substitution. "Vac" represents a vacancy.

| $2Sn^{2+}$ @ $2Ag^{+}$ → $2Ag^{+}$ vac and $Sn^{4+}$ @ $Bi^{3+}$ → $Ag^{+}$ vac | |
|---|---|
| Site coordinates | Substitution |
| Ag: (0.0, 0.0, 0.0) | Sn |
| Ag: (0.0, 0.25, 0.25) | Sn |
| Bi: (0.5, 0.0, 0.25) | Sn |
| Ag: (0.0, 0.5, 0.0) | vac |
| Ag: (0.25, 0.25, 0.0) | vac |
| Ag: (0.25, 0.0, 0.25) | vac |

**Table S10.** Expected (from solution concentration) versus observed values via XPS of relative concentrations of Sn, Cs, Ag, Bi, and Br in thin films of **1:Sn**. Observed values were calculated using the MultiPak software suite for XPS data analysis. Systematic discrepancies between expected (solution) and observed (film) values are due to difficulties with consistent fitting of peaks from element to element and the possibility of imperfect transfer of precursors from the solution to the film while spincoating. All values are given in atom percent.

| Sn in solution | Sn in film | Cs in solution | Cs in film | Ag in solution | Ag in film | Bi in solution | Bi in film | Br in solution | Br in film |
|---|---|---|---|---|---|---|---|---|---|
| 0 | 0 | 20 | 27.7 | 10 | 8.4 | 10 | 13.1 | 60 | 50.9 |
| 1 | 1.9 | 20 | 23.0 | 9.5 | 15.2 | 9.5 | 10.4 | 60 | 49.6 |
| 2 | 2.6 | 20 | 22.4 | 9.0 | 12.9 | 9.0 | 11.0 | 60 | 51.2 |
| 3 | 3.4 | 20 | 22.4 | 8.5 | 9.8 | 8.5 | 11.1 | 60 | 53.3 |
| 4 | 4.4 | 20 | 23.3 | 8.0 | 9.4 | 8.0 | 9.9 | 60 | 53.0 |

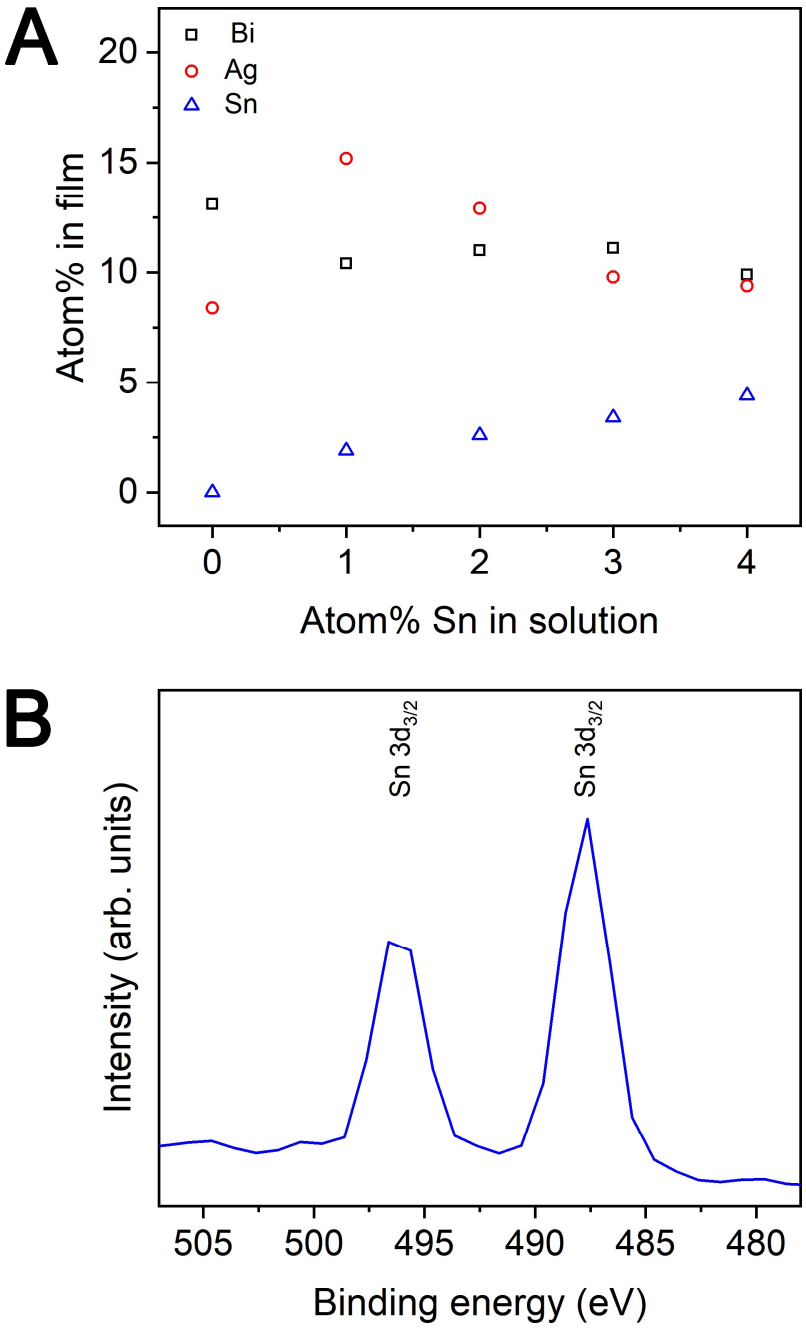


**Figure S19.** A) Concentrations of Ag, Bi, and Sn in thin films of **1:Sn** as determined by XPS versus concentration of Sn in the precursor solution. B) The Sn 3d photoemission peaks observed by XPS in a thin film of **1:Sn** synthesized from a precursor solution containing 4 atom% Sn.

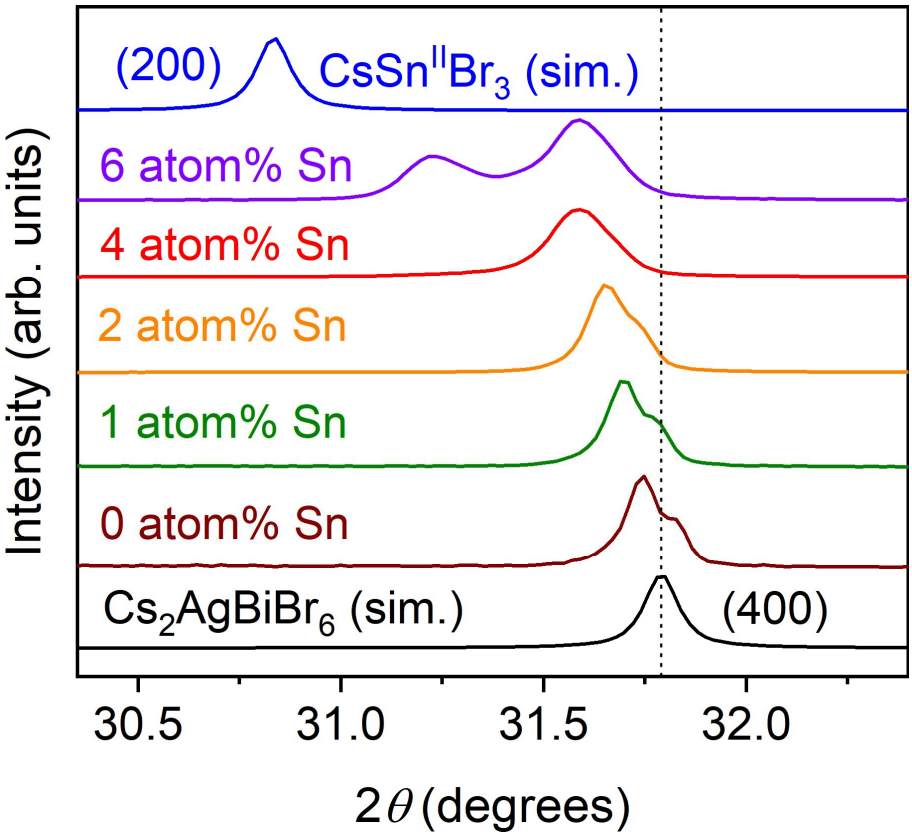


**Figure S20.** XRD patterns measured on thin films of **1:Sn**. The percent values indicate the overall atom% of Sn in the precursor solution. The dotted line is aligned with the (400) reflection of **1** to emphasize the 2$\theta$ shift of the peaks with Sn alloying. The peak splitting observed is due to the Cu-K$\alpha_1$ and Cu-K$\alpha_2$ emission lines. Phase purity is maintained until ≥4 atom% Sn.

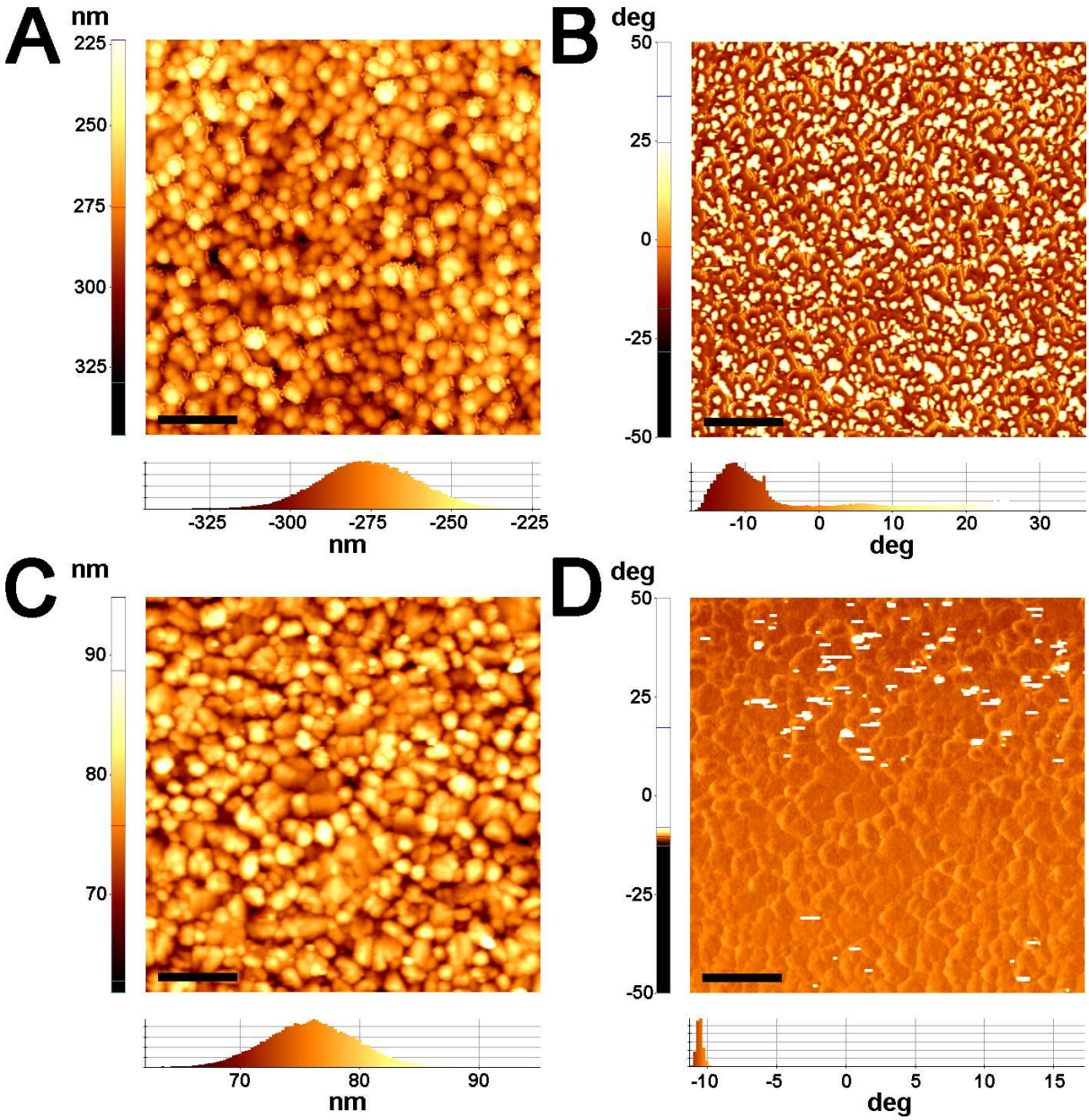


**Figure S21.** Representative AFM images of thin films of A & B) **1** and C & D) **1:Sn** (4 atom% Sn) showing the A & C) topography and B & D) phase. The scale bar in each image is 400 nm.

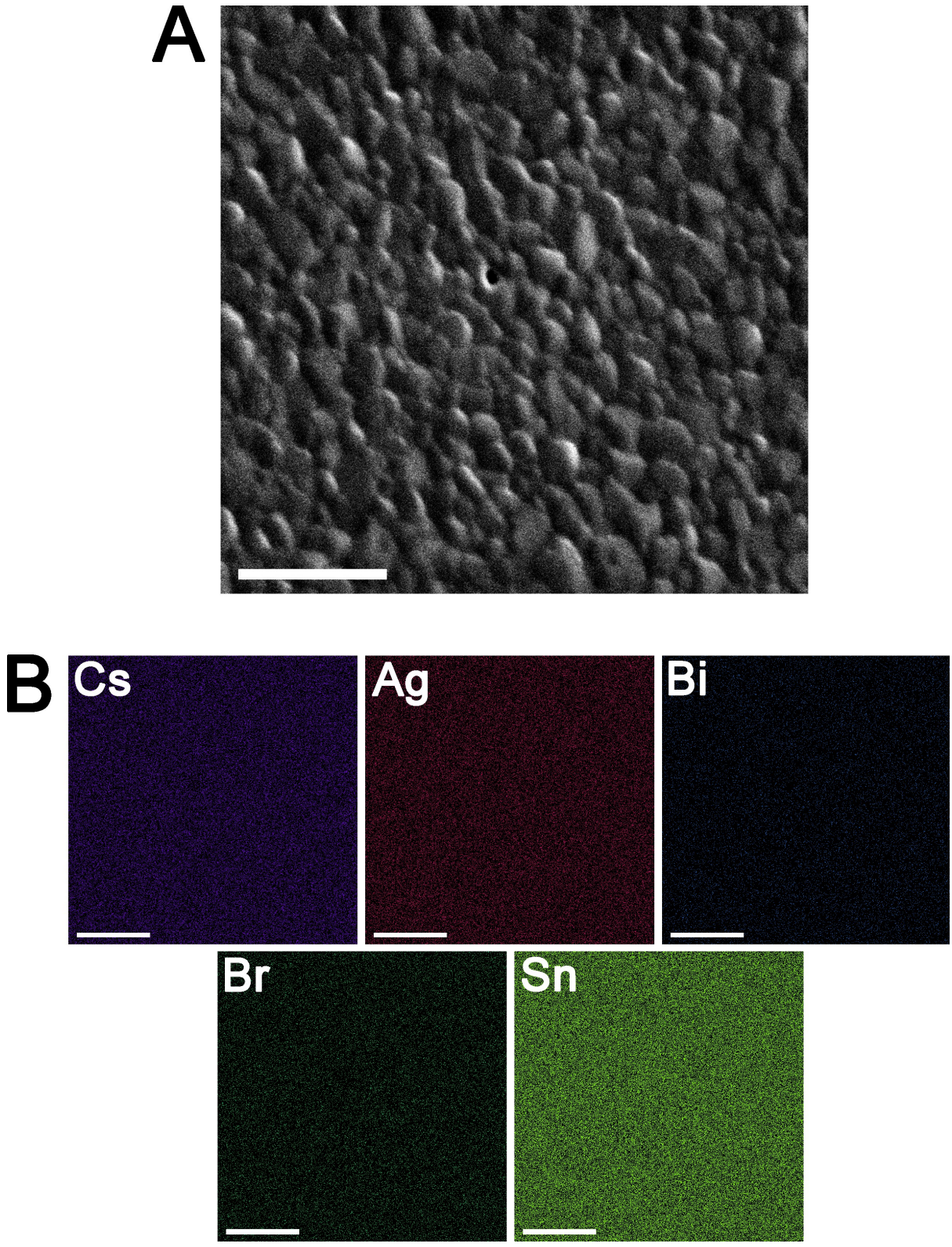


**Figure S22.** A) A representative SEM image of a thin film of **1:Sn** (4 atom% Sn). B) Elemental mapping on the same area shown in A) using EDX. The scale bar in each image is 2 μm.

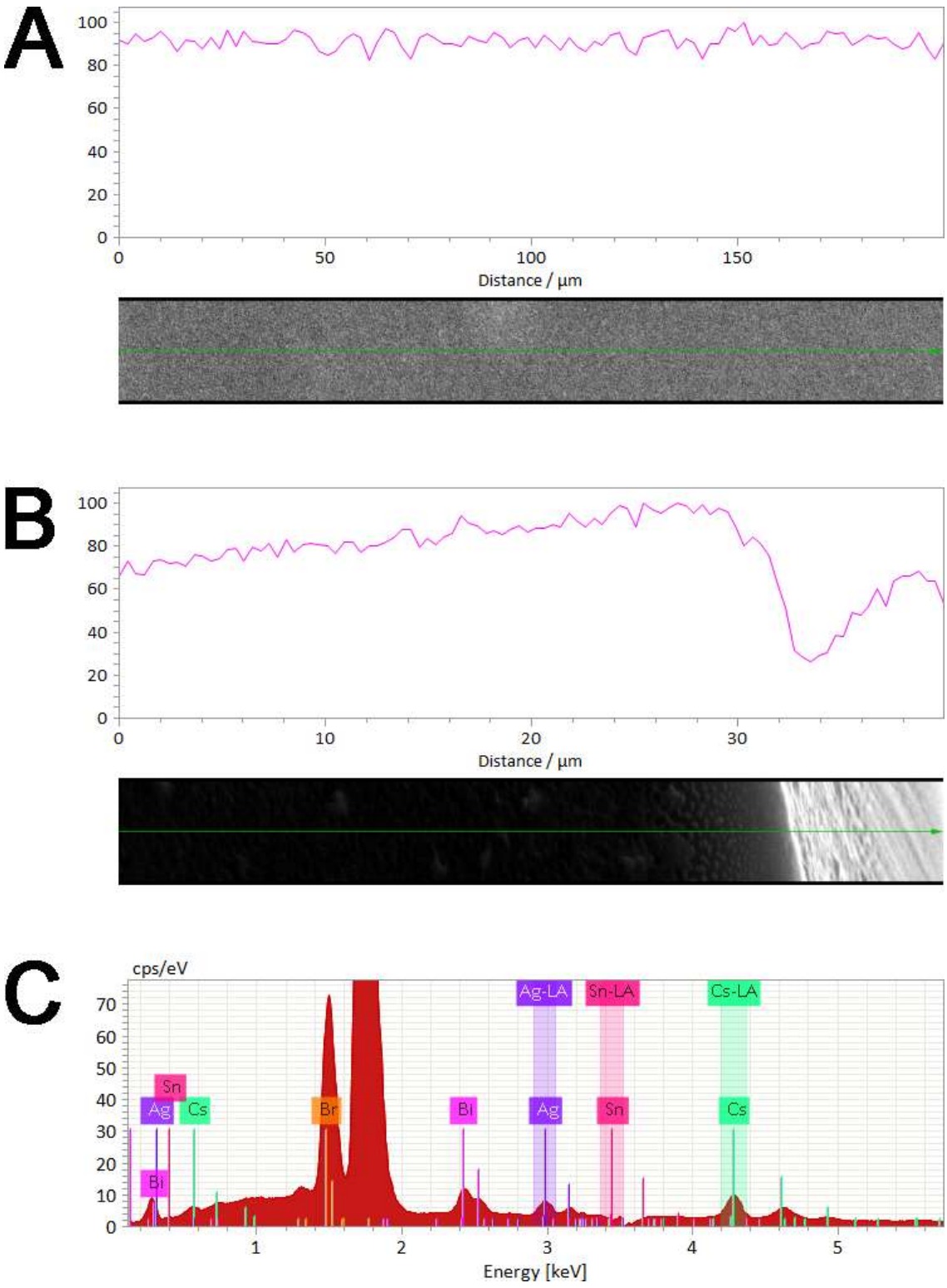


**Figure S23.** Representative EDX line scans measuring Sn content and corresponding secondary electron images taken A) in the center of a thin film of **1:Sn** (4 atom% Sn) and B) on the edge of a thin film of **1:Sn** (4 atom% Sn). C) A representative EDX spectrum. The intense peak at 1.8 keV in C) is due to the Si substrate.

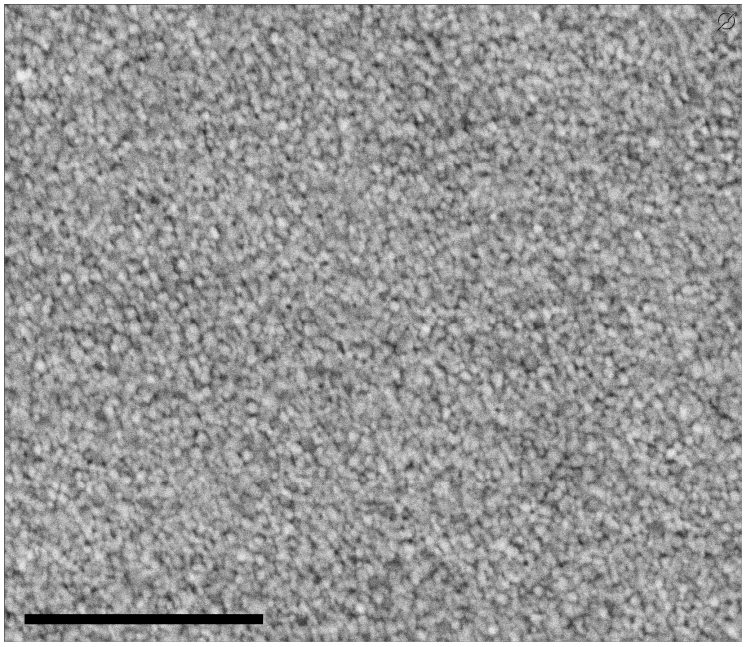

**Figure S24.** A representative CBS image of a thin film of **1:Sn** (4 atom% Sn). The scale bar is 4 μm.

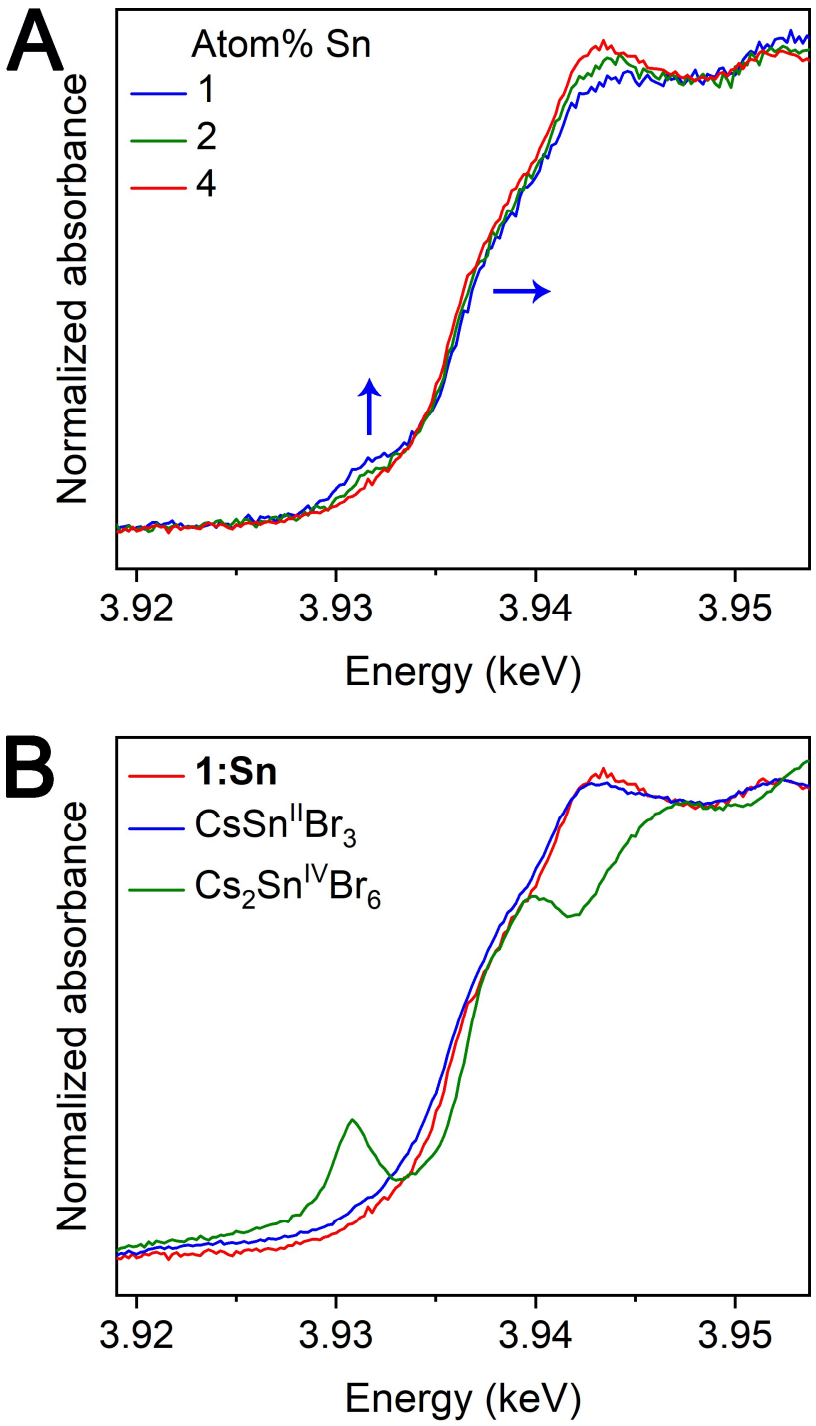


**Figure S25.** Sn $L_3$-edge XANES spectra of thin films of **1:Sn** measured under inert conditions. The thin film of **1:Sn** in B) contains 4 atom% Sn.

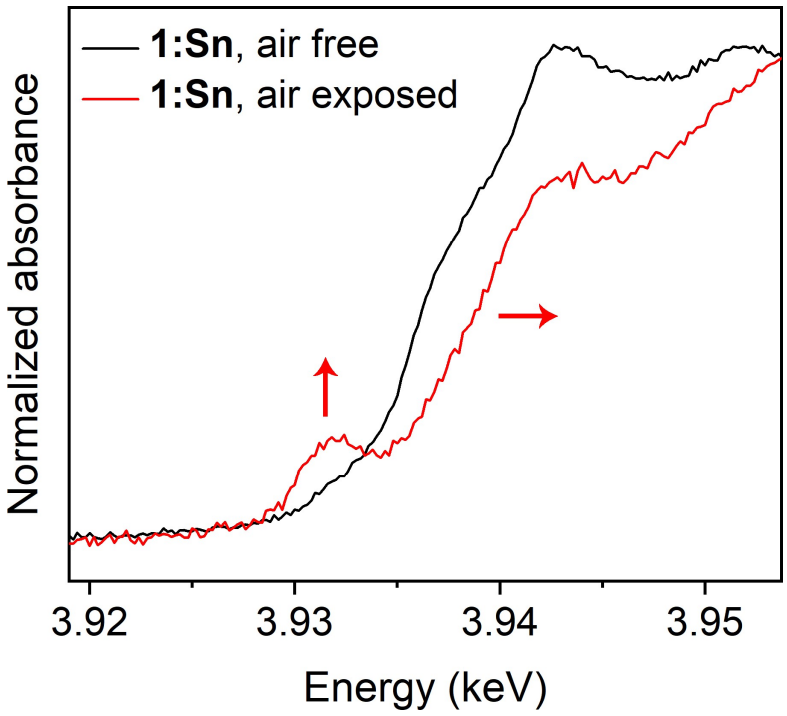


**Figure S26.** Sn $L_3$-edge XANES spectra of a thin film of **1:Sn** (4 atom% Sn) before and after exposure to ambient atmosphere overnight.

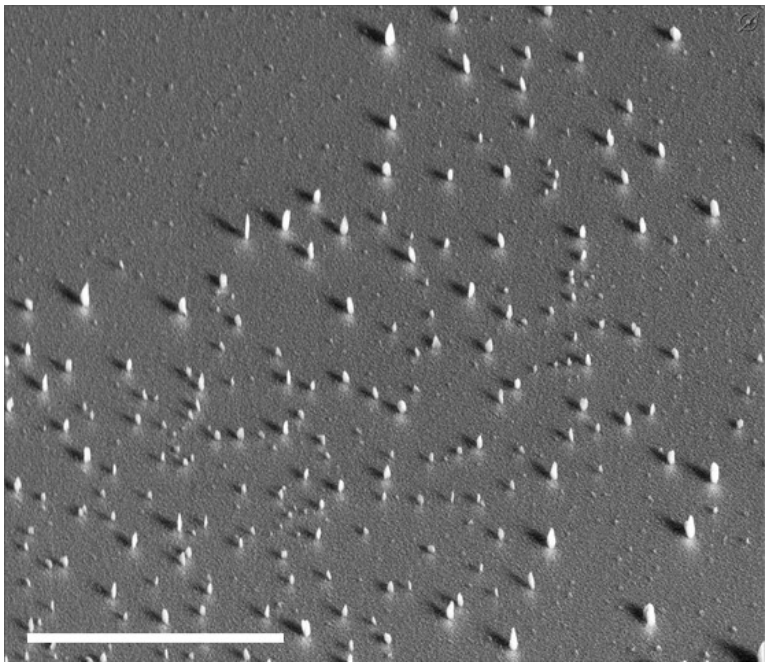

**Figure S27.** A representative SEM image of a thin film of **1:Sn** (4 atom% Sn) that was heated at 60 ºC in air for 48 h. The scale bar is 20 μm.

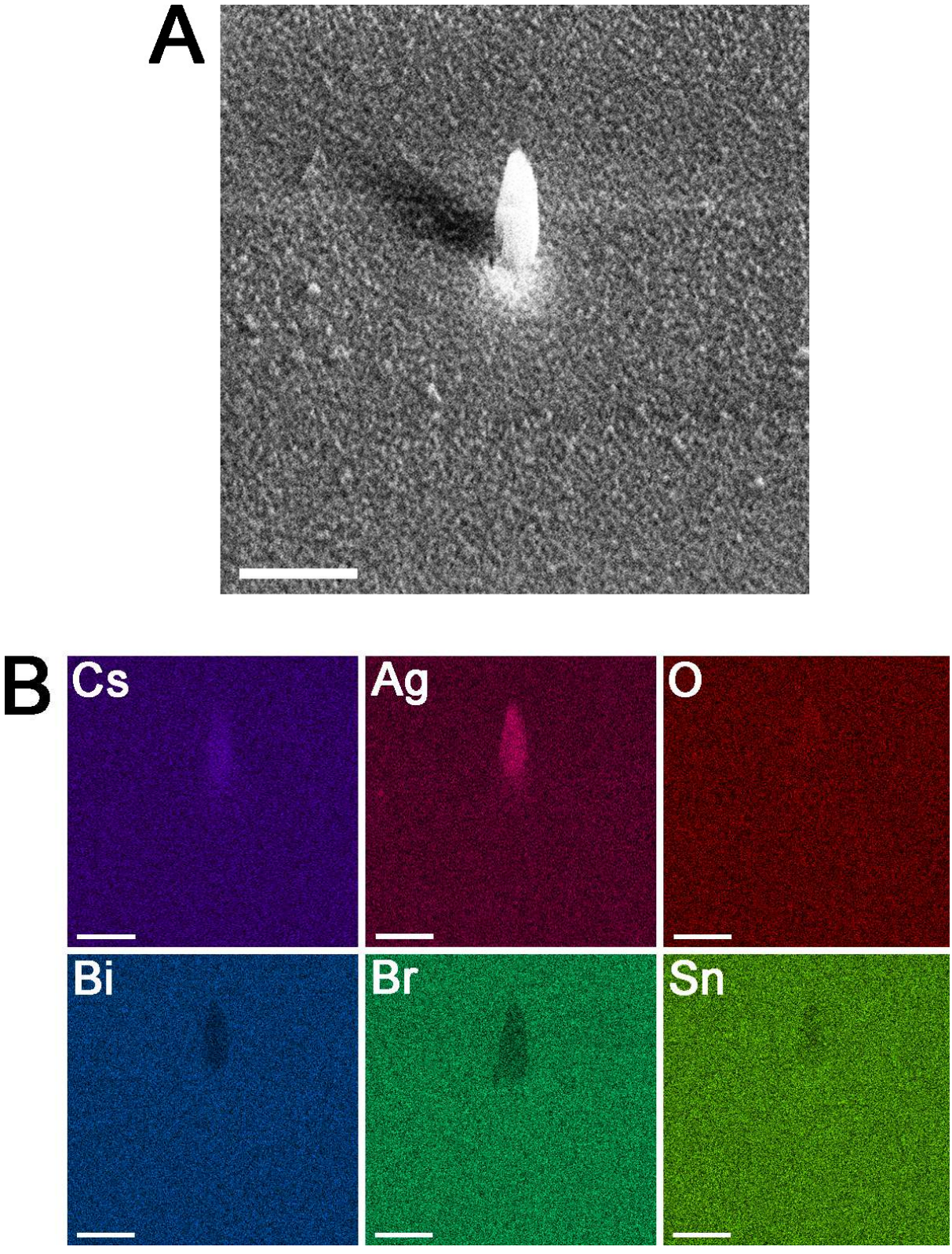


**Figure S28.** A) An SEM image of a surface feature on an oxidized thin film of **1:Sn** (4 atom% Sn). B) Elemental mapping on the same area shown in A) using EDX, showing highly elevated levels of Ag and slightly elevated levels of Cs and O localized at the surface feature. The scale bar in each image is 3 μm.

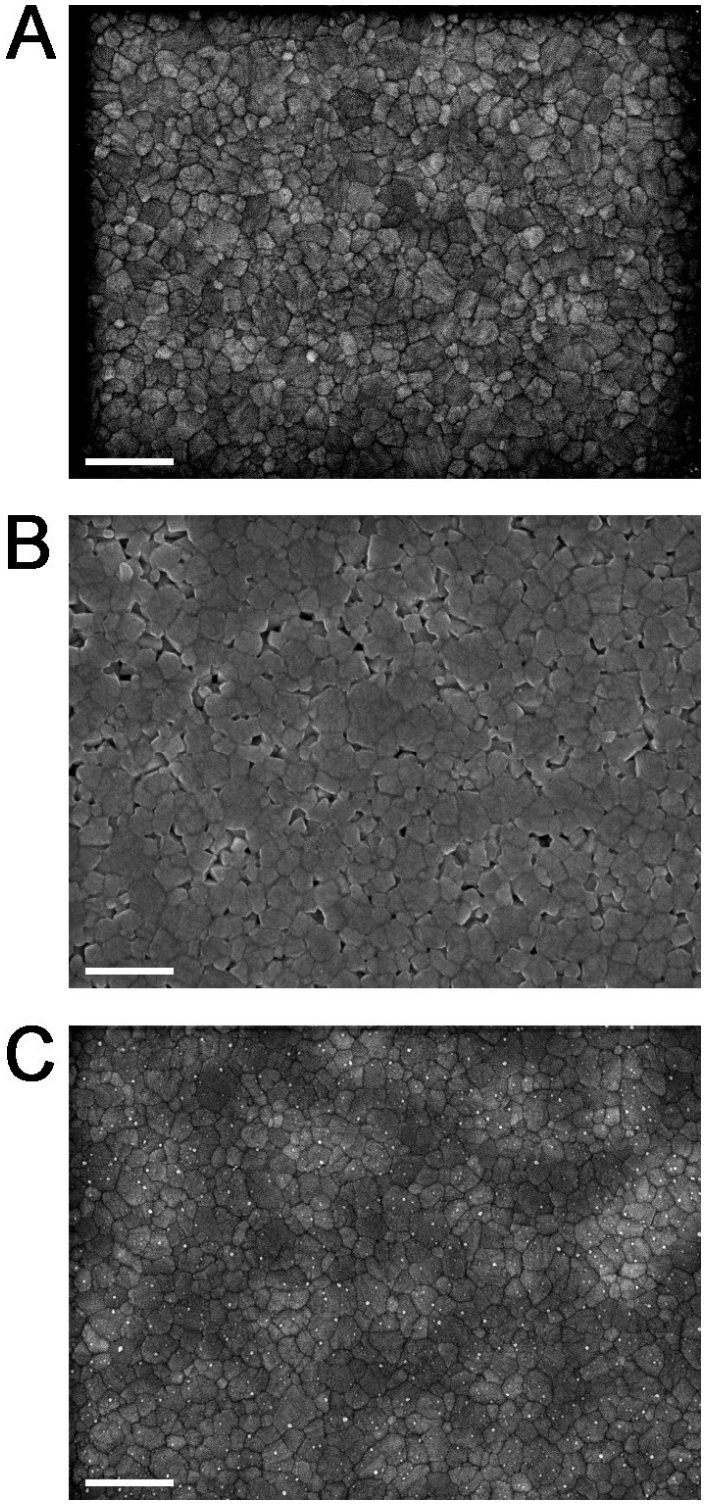


**Figure S29.** SEM images of thin films of **1:Sn** (4 atom% Sn) taken A) air free, B) after exposure to $N_2$ saturated with $H_2O$, and C) after exposure to dry air. The scale bar in each image is 500 nm.

**References**


1. A. H. Slavney, T. Hu, A. M. Lindenberg and H. I. Karunadasa, *J. Am. Chem. Soc.*, 2016, **138**, 2138-2141.
2. D. E. Scaife, P. F. Weller and W. G. Fisher, *J. Solid State Chem.*, 1974, **9**, 308-314.
3. B. Lee, C. C. Stoumpos, N. Zhou, F. Hao, C. Malliakas, C.-Y. Yeh, T. J. Marks, M. G. Kanatzidis and R. P. H. Chang, *J. Am. Chem. Soc.*, 2014, **136**, 15379-15385.
4. J. C. Gupta and S. P. Srivastava, *Anal. Bioanal. Chem.*, 1962, **191**, 267-273.
5. Bruker, SAINT and SADABS, Bruker AXS Inc., Madison, WI, 2016.
6. G. M. Sheldrick, *Acta Crystallogr., Sect. A: Found. Crystallogr.*, 2008, **64**, 112-122.
7. G. M. Sheldrick, in *SHELXL-97, A Program for Crystal Structure Refinement*, Göttingen, 1997.
8. O. V. Dolomanov, L. J. Bourhis, R. J. Gildea, J. A. K. Howard and H. Puschmann, *J. Appl. Crystallogr.*, 2009, **42**, 339-341.
9. P. Müller, R. Herbst-Irmer, A. L. Spek, T. R. Schneider and M. R. Sawaya, *Crystal Structure Refinement: A Crystallographer's Guide to SHELXL*, Oxford University Press, Oxford, 2006.
10. R. A. Konetzki and Y. A. Chang, *J. Mater. Res.*, 1988, **3**, 466-470.
11. B. Ravel and M. Newville, *J. Synchrotron Radiat.*, 2005, **12**, 537-541.
12. P. Kubelka and F. Z. Munk, *Z. Tech. Phys.*, 1931, **12**, 593-601.
13. A. H. Slavney, L. Leppert, D. Bartesaghi, A. Gold-Parker, M. F. Toney, T. J. Savenije, J. B. Neaton and H. I. Karunadasa, *J. Am. Chem. Soc.*, 2017, **139**, 5015-5018.
14. K. Vandewal, S. Albrecht, E. T. Hoke, K. R. Graham, J. Widmer, J. D. Douglas, M. Schubert, W. R. Mateker, J. T. Bloking, G. F. Burkhard, A. Sellinger, J. M. J. Fréchet, A. Amassian, M. K. Riede, M. D. McGehee, D. Neher and A. Salleo, *Nat. Mater.*, 2013, **13**, 63.
15. E. Buchaca-Domingo, K. Vandewal, Z. Fei, S. E. Watkins, F. H. Scholes, J. H. Bannock, J. C. de Mello, L. J. Richter, D. M. DeLongchamp, A. Amassian, M. Heeney, A. Salleo and N. Stingelin, *J. Am. Chem. Soc.*, 2015, **137**, 5256-5259.
16. J. P. Perdew, K. Burke and M. Ernzerhof, *Phys. Rev. Lett.*, 1996, **77**, 3865-3868.
17. G. Kresse and J. Furthmüller, *Phys. Rev. B*, 1996, **54**, 11169-11186.